TÉCNICO LISBOA

Development of methods for damage Identification in laminated composite structures

Tomás Miguel Pargana e Oliveira

Thesis to obtain the Master of Science Degree in

Aerospace Engineering

Supervisor: Prof. Dr. José Viriato Araújo dos Santos

Examination Committee

Chairperson: Prof. Dr. Filipe Szolnoky Ramos Pinto Cunha
Supervisor: Prof. Dr. José Viriato Araújo dos Santos
Member of the Committee: Prof. Dr. Hugo Filipe Diniz Policarpo

December 2021

Declaration

I declare that this document is an original work of my own authorship and that it fulfills all the requirements of the Code of Conduct and Good Practices of the Universidade de Lisboa.

To my family...

”...it’s time that we began

to laugh and cry and cry and laugh about it all again.”

Acknowledgments

On the end of a long and eventful learning experience in IST, I would like to leave a few word of appreciation to those who have impacted my life and helped me reach this milestone. This is definitely a path that is not taken alone, and without you I wouldn't be where I am today.

I want to start by thanking my thesis supervisor, Prof. José Viriato dos Santos, for the guidance and challenges you have put in my path, which have allowed me to gain a renewed appreciation for the engineering process and a greater pride in accomplishing this work.

To all my colleagues with whom I have shared group projects, desks, notes, or an earned moment of break from the pressure, thank you for taking part in this path. It isn't easy earning this degree, but it gets a little less hard with company.

To the friends and partners in this journey that I have in TUIST, thank you for all the moments where we grew together through the music we made.

Ana, thank you for being by my side everyday. You deserve a good part of the credit for this achievement.

And finally, thank you to my family. You are the reason I try to be better every day.

Resumo

Os materiais compósitos laminados são um marco do desenvolvimento moderno de materiais, com fibras mais fortes que a maioria dos materiais convencionais combinadas com resinas para formar estruturas de engenharia versáteis e eficientes. O avanços no desenvolvimento dos materiais devem ser acompanhados por métodos igualmente avançados para deteção de dano, dado que estes materiais desenvolvem modos de falha inerentemente únicos. Esta tese procura desenvolver o estudo do uso de formas modais e as suas derivadas espaciais para fazer deteção e localização de dano em placas compósitas laminadas retangulares. O software comercial ANSYS® Parametric Design Language (APDL) é usado para fazer simulações de Elementos Finitos das placas, com diversos cenários e modelos mecânicos de dano. O software Matlab® é usado para pós-processar os resultados das simulações, nomeadamente no cálculo das derivadas usando o Método das Diferenças Finitas, e aplicação de três índices de dano, um dos quais proposto nesta tese. De forma a imitar condições experimentais, e para testar a resiliência dos diferentes graus de derivação, diferentes níveis de ruído são introduzidos nos resultados das simulações de Elementos Finitos. Um Índice de Qualidade é usado para avaliar quantitativamente as soluções, principalmente da resposta ao ruído introduzido. Os resultados mostram que os diferentes métodos de deteção de dano alcançam resultados comparáveis em termos de qualidade, com maior sucesso quando a análise é feita modo a modo, com penalização na simplicidade da análise. Os resultados também indicam que a detetabilidade de dano é maior quando as áreas danificadas coincidem com zonas de maior deslocamento das formas modais, e que níveis de ruído mais elevados têm um impacto negativo mais notável quando as derivadas de grau mais elevado são aplicadas.

Palavras-chave: Compósitos laminados, Análise modal, Simulação de ruído, Elementos finitos, Localização de dano, Diferenças finitas

Abstract

Laminated composite materials are a staple of modern material development, with fibers stronger than most conventional materials being combined with resins to form versatile and efficient engineering structures. However, the advancements in material development must be accompanied by equally advanced methods for damage detection, as these materials develop inherently unique failure modes. This thesis aims to further the study of the use of modal shapes and their spatial derivatives to perform damage localization in laminated composite rectangular plates. Ansys® Parametric Design Language (APDL) is used to perform Finite Element simulations of plates with several damage scenarios and damage mechanics models. Matlab® is used to post-process these simulations results, namely by calculating the derivatives using the Finite Difference Method, and applying three different Damage Indexes, including one that is being proposed here. To mimic experimental conditions and testing the resilience of the derivatives degrees, different noise levels are introduced in the results of the Finite Element simulations. A Quality Index is employed to quantitatively evaluate the solutions, mainly regarding the response to the introduced noise. The results show that the different Damage Detection Methods tested have comparable results in terms of quality with a higher degree of success when the analysis is made mode by mode, with a penalty in simplicity of analysis. These results also show that the damage detectability is higher when the damaged areas coincide with high displacement areas of the mode shapes and that higher noise levels have a more noticeable negative impact when employing higher order derivatives.

Keywords: Laminated composites; Modal analysis; Noise simulation; Finite elements; Damage localization; Finite Differences

Contents

Acknowledgments vii
Resumo ix
Abstract xi
List of Tables xv
List of Figures xvii
Nomenclature xix
Glossary xxiii

1 Introduction **1**
1.1 Motivation and objectives 1
1.2 State of the art 3
1.3 Thesis outline 4

2 Theoretical background **5**
2.1 Laminated composite materials 5
2.2 Natural frequencies and mode shapes 10
2.3 Finite Element Method 11
2.4 Damage Models 12
2.4.1 Microphenomenology 12
2.4.2 Reduction of the Laminated Stiffness 13
2.4.3 Teflon® tape inclusion 14
2.5 Finite Difference Method 15
2.6 Damage indices 15
2.6.1 Difference in Field Derivatives 16
2.6.2 Translation, Slope, and Curvature Differences 16
2.6.3 Sum of Field Derivatives 17

3 Implementation **19**
3.1 Finite Element Model 19
3.1.1 APDL® algorithm 19
3.1.2 Damage Simulation 21
3.2 Results post-processing 22

3.2.1 Finite Differences . . . 22
3.2.2 Noise simulation . . . 23
3.2.3 Results quality index . . . 23
3.3 Simulation and analysis data . . . 24
3.3.1 Plate properties . . . 24
3.3.2 Element sizing in the FE simulations . . . 24
3.3.3 Damage Mechanics . . . 26
3.3.4 Damage indicators . . . 27
3.3.5 Noise Inclusion . . . 27

4 Results **29**
4.1 Element size analysis . . . 29
4.2 Damage Mechanics Analysis . . . 30
4.3 Damage indices . . . 33
4.3.1 Difference in Field Derivatives . . . 34
4.3.2 Differences between sums of Displacements, Rotations and Curvatures . . . 37
4.3.3 Sum of Field Derivatives . . . 42
4.4 Frequency Analysis . . . 47
4.5 Influence of noise on damage detection . . . 49
4.6 Influence of damage depth in the plate on damage detection . . . 53

5 Conclusions **55**
5.1 Achievements . . . 55
5.2 Future Work . . . 57

Bibliography **59**

List of Tables

2.1 Damage Parameters use in the Microphenomenology damage model 13

3.1 Plate properties 25
3.2 Element sizes and number of nodes for the simulations 25
3.3 Damage models and parameters study 26

4.1 Natural frequency comparison for DC8 and DC17 and center damage scenario 48

List of Figures

1.1 Comparative overview of material properties between composites and metals. [1] 2
1.2 Displacement, curvature, and fourth derivative of the first mode of a damaged beam.[10] . 4

2.1 Laminate layers schematics 8

3.1 Flowchart describing the APDL® modelling process 20

4.1 Computation time according to element size 29
4.2 First mode curvatures for different element sizes. 30
4.3 Damage Detection for Damage Case 1 31
4.4 Damage Detection using Translation Differences 31
4.5 Damage cases severity study 32
4.6 Displacement fields without damage for the first ten modes of the clamped plate. 33
4.7 Displacement fields without damage for the first ten modes of the free plate. 33
4.8 First four derivatives of the displacement for the selected modes of the damaged plate with DC8 and center damage scenario, using the x component of the derivation vectors. . 34
4.9 Damage detection with the DFD index for DC8 and center damage scenario. 36
4.10 Damage detection with the DFD index for DC8 and corner damage scenario, for the plate with clamped edges. 37
4.11 Damage detection with the DFD index for DC8 and center + corner damage scenario, for the plate with clamped edges. 38
4.12 Damage detection with the DFD index for DC8 and center + corner damage scenario, for the free plate. 39
4.13 Displacement field and first two derivatives of the undamaged and damaged plate with both DC8 and DC17, and center damage scenario, using the euclidean norm of the derivation vectors, for the plate with clamped edges. 39
4.14 Displacement field and first two derivatives of the undamaged and damaged plate with both DC8 and DC17, and center damage scenario, using the euclidean norm of the derivation vectors, for the free plate. 40
4.15 Damage detection with the TD, SD and CD index for DC8 and DC17, and center damage scenario, for both the plate with clamped edges and the free plate. 41

4.16 Damage detection with the TD, SD and CD index for DC8 and DC17, and corner damage scenario, for both the plate with clamped edges and the free plate. 42
4.17 Damage detection with the TD, SD and CD index for DC8 and DC17, and center + corner damage scenario, for both the plate with clamped edges and the free plate. 43
4.18 Displacement field and first two derivatives of the undamaged and damaged plate with both DC8 and DC17, and center damage scenario, using the x component of the derivation vectors, for the plate with clamped edges. 44
4.19 Displacement field and first two derivatives of the undamaged and damaged plate with both DC8 and DC17, and center damage scenario, using the x component of the derivation vectors, for the free plate. 44
4.20 Damage detection with the DFD method for DC8 and DC17 and center damage scenario, for both the clamped and free plates. 45
4.21 Damage detection with the DFD index for DC8 and DC17 and corner damage scenario, for both the plate with clamped edges and the free plate. 46
4.22 Damage detection with the DFD index for DC8 and DC17 and center + corner damage scenario, for both the plate with clamped edges and the free plate. 47
4.23 Average values of the displacement, rotation, and curvature on the damaged area *vs.* frequency difference for both border conditions and the first ten modes. 48
4.24 The four derivation degrees employed and their response to the noise levels, for Damage Case 8. 50
4.25 The four derivation degrees employed and their response to the noise levels, for Damage Case 8 and center damaged area, using the sum of the first ten modes 51
4.26 Damage detection with different damage placements, severity, and noise level, for detection quality close to μ_c. 52
4.27 Behaviour of the quality index for different values of the Noise Level, and for two different damage cases 53
4.28 Damage severity according to damage depth. 54

Nomenclature

Greek symbols

κ	Curvature.
μ	Quality index.
ν	Poisson's Ratio.
σ	Stress.
θ	Rotation.
ε	Strain.

Roman symbols

$[A]$	Extensional stiffness matrix.
$[B]$	Bending stiffness matrix.
$[C]$	Stiffness matrix.
$[D]$	Bending-extensional coupling stiffness matrix.
$[Q]$	Plane stress reduced matrix.
$[R]$	Transformation matrix.
$[S]$	Compliance matrix.
$\tilde{A}$	Property A of a damaged plate.
d	Shear damage parameter - Microphenomenology model.
d'	Transverse damage parameter - Microphenomenology model.
$d^{(e)}$	Damage parameter - RLS model.
E_1	Young's modulus in the fiber direction.
E_2	Young's modulus in the transverse direction.
G_{12}	In-plane shear modulus.

v_A Volume fraction of component A.

w Transverse displacement.

Subscripts

$1, 2$ Longitudinal and transverse directions.

f Fibers.

m Matrix.

q Mode.

x, y, z Cartesian components.

Glossary

APDL® Ansys® Parametric Design Language. 19

Damage Case Specific manipulation of the elastic constants in the damaged area. 10

Damage Scenario Specific placement and size of the damaged area. 25

DFD Damage index - Difference of Field Derivatives. 16

FEM Finite Element Method. 11

NL Noise Level. 23

RLS Reduction of Laminated Stiffness. 13

SFD Damage index - Sum of Field Derivatives. 17

SNR Signal-to-noise ratio. 23

TD, SD and CD Damage index - Translation, Slope, and Curvature Differences. 16

Chapter 1

Introduction

1.1 Motivation and objectives

Composite materials have been having a growing impact in several areas of manufacture industries in the past decades, and the importance of having the right insight about them has naturally been growing as well. From aviation, to sports equipment, and all areas of engineering development, the competitive advantages of most commercial composite materials are clear to anyone considering the optimal material to develop and build a structure, namely for their stiffness *versus* weight (specific strength) characteristics, with their high cost being the main disadvantage. Figure 1.1 shows a general overview of the main qualities of interest for material selection, as expressed by Strong [1], and how composite materials are vastly superior in most cases. Some notable examples of the successful application of composite materials include the Boeing 787 commercial aircraft, whose construction is composed by 50% composite materials [2] and is one of the most efficient on the market, and the McLaren P1 2014 road sports car, whose carbon fiber structure was deemed so solid that a roll cage was not considered necessary for race conditions [3].

By definition, a composite material is the result of the combination of two or more different materials, with different properties. Laminated composite materials are a specific case of those, and the subject of this thesis. Composite laminates are typically composed of two materials: the matrix, usually a polymer or resin, and the fibers, most commonly carbon or glass; these fibers are selected for their a tensile strength many times superior of that of commonly used materials. However, as is the nature of most fibers, they lack any significant structural rigidity on their own. For this reason, the employment of resin to aggregate the fibers in specific orientations contributes to the structural integrity, the transverse rigidity and the even transfer of loads to all fibers. Composite laminates are built by superimposing several plies of this composite material. This feature also leads to one of the main failure cases for laminated composites: delamination, which consists of a localized failure in the connection between two layers. This type of damage, along with other cases originated from the use of the structures, is sometimes extremely difficult to detect, locate and quantify, especially if not visible to the naked eye.

Structural health monitoring is the practise of conducting tests or routines that assess the state of

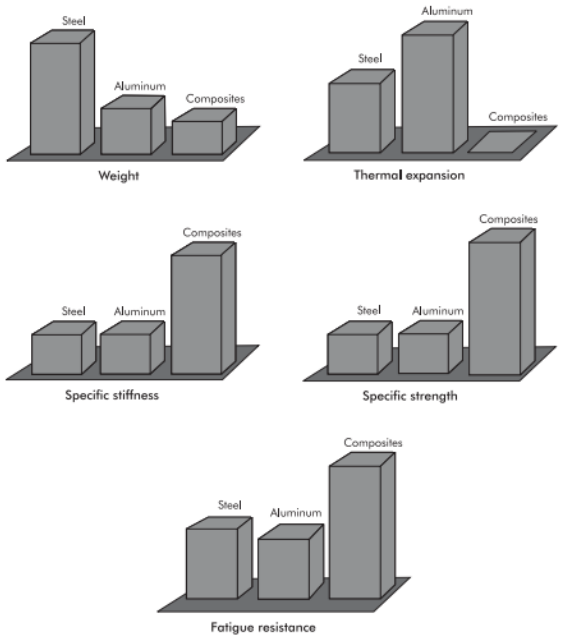

Figure 1.1: Comparative overview of material properties between composites and metals. [1]

engineering components or systems, regarding their intended use [4], through non-destructive methods. Vibration-based methods have been employed for damage detection in structures for a few decades [5]. These generally compare the dynamic behaviour of a structure with and without damage, using various techniques. The object of this thesis is specifically modal analysis, which studies the mode shapes produced by the structures when subjected to stimuli at specific frequencies, called natural frequencies. The process of damage detection is based on having a baseline behaviour for a healthy plate and comparing it to one which is damaged. This information either comes from experimental data or from Finite Elements simulations. For this thesis Finite Element simulations are run with different variables being manipulated in order to have a broader array of cases to analyze.

In modal analysis based damage detection, an often used approach is to calculate spatial derivatives of mode shapes [6–8], as this process has the potential to highlight seemingly minor imperfections in the mode shapes - which are normally smooth sinusoidal shapes - that can indicate the presence of damage. The application of this approach depends on a number of factors, such as a uniform grid of FE nodes or data points, however it has been shown to be useful and accurate in damage detection and localization. The mathematical technique most commonly used to calculate these derivatives is the Finite Difference Method, and it is the one employed in this thesis.

A variable being tested is the influence damage depth has on the detection. As the existence of damage on the middle layers of a laminated composite plate represents a higher degree of difficulty for detection by visual analysis, the validation of the chosen techniques for detecting this type of damage should have an important impact on their application.

The objective of this thesis is then to encompass these techniques - FE simulations, modal analysis, spacial differentiation - to detect and locate damage in composite plates, in order to contribute to a better

understanding and safer use of these remarkable materials. This can be seen as an inverse problem, where the damage detection is expected, but the best way to achieve it is the objective.

1.2 State of the art

Within the context of structural health monitoring of composite plates using modal analysis and finite differences, the routines adopted in this work are contextualized in a considerable body of work, which has been developed for a few decades.

In 1991, Pandey et al. [7] first proposed the use of the curvatures of mode shapes - second derivatives -, calculated using finite differences, for damage detection and localization in beams, where the improvement of damage detection *versus* the use of the modal displacements is noted, for numerical simulation data; the implementation of both mode shapes and spatial derivatives is essentially the same as the ones that follow, including the work presented in this thesis. This method was then used in 1999 by Abdel Wahab and De Roeck [9] in simulated as well as experimental data, with promising results, limited mainly by the quality of the measured data; here, the authors applied the technique to data measured from an existing bridge, thus demonstrating a promising practical application of the use of modal curvatures; a damage detection method was also proposed, which consisted on using only the damaged component's data and recreating the undamaged mode shapes by applying a smoothing algorithm to the damaged ones. In 2008, Whalen [10] expanded the analysis of the use of different derivative degrees for damage detection in beams; Figure 1.2 shows the impact that a damaged area on a beam has on the derivatives of the mode shapes: as the higher derivation degrees are employed, the disturbance caused by the damage reaches several orders of magnitude higher values than the original values of the derivatives, while in the displacements the damage is not even noticeable. In 2005, Sazonov and Klinkhachorn [11] deepened the usefulness of the use of modal curvatures by establishing a method for optimal spatial sampling intervals in beams, which is equivalent to the selection of element size in Finite Element simulations; this analysis was also performed by Moreno-García et al. [8] in 2014, although for plates. This aspect has an impact in both numerical and experimental applications of the finite difference method, as both are limited in their precision, and because the computation time and resources needed are always a factor to consider.

In 2006, Araújo dos Santos et al. [6] applied the finite element method to compute the curvatures of the mode shapes of a laminated composite plate, obtained via experiments. In this study, the detected damage was made by impact, while for the ones featuring aluminum bars it was composed of milled slots, which highlights the importance of understanding the unique characteristics of this type of material. Other papers also applied the use of curvatures calculated from finite differences for damage detection on experimental data, with successful results [12–16]. No examples of the study of the influence of damage depth on detection were found.

The reviewed literature shows a continued effort in developing the use of the aforementioned techniques for practical applications, as well as promoting a deeper understanding of all the considerations needed when applying them. Both of these aspects are discussed in the following chapters.

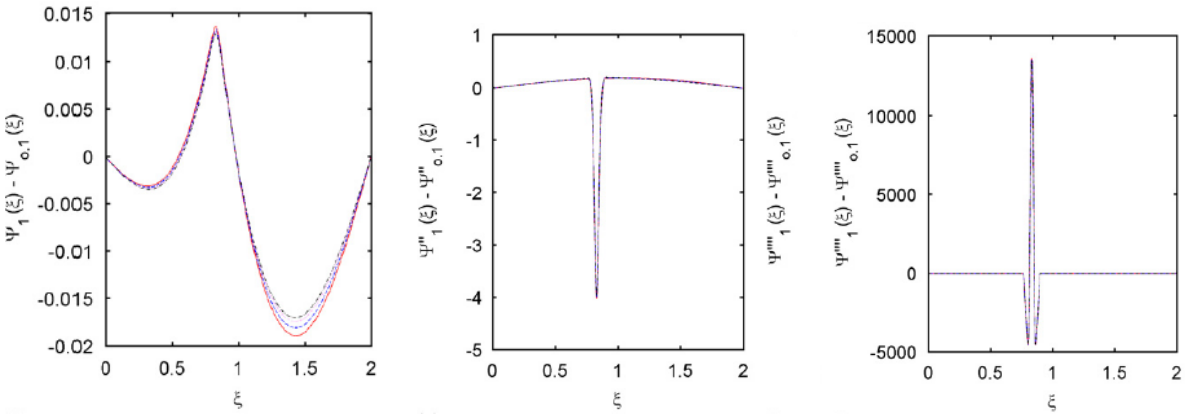

(a) Displacements (b) Curvature (c) Fourth derivative

Figure 1.2: Displacement, curvature, and fourth derivative of the first mode of a damaged beam.[10]

1.3 Thesis outline

After this introductory chapter, follows Chapter 2, where the theoretical introduction to the fundamental concepts approached in this thesis is made: important concepts and governing laws for composite laminates, the basis for modal analysis, the Finite Element Method, damage mechanics and FE models, the Finite Difference Method, and the employed damage indices are presented.

On Chapter 3, the implementation of these concepts with the required software tools is explained. First, the use of Ansys APDL® to implement the FE model and then Matlab® to post-process the data. As there is a considerable number of variables to explore, a scheme of the simulations and processing runs is designed.

On Chapter 4, the results are presented and discussed. The different variables, regarding the simulations, data collecting and post-processing, are analysed to propose optimal solutions for the problem at hand.

Finally, on Chapter 5, the achievements and shortcomings of the approaches presented in this thesis are analysed, final conclusions are drawn, as well as a projection for future work in this area of study.

Chapter 2

Theoretical background

In this thesis, the damage detection methods used are all based on the analysis of mode shapes on a rectangular laminated composite plate. Different plate setups are modelled in order to establish a comparison with the different methods employed in each case. The choice towards the use of a rectangular plate is made for a greater simplicity, versatility of applications of these techniques, as well as a greater ease in the comparisons with previous studies which have featured the same choice. Furthermore, rectangular plates are members used in several engineering structures. Finite Element simulations are designed and employ and test the chosen models and techniques. The post-processing of the mode shapes was carried out using the Finite Difference Method to find spatial derivatives in different ways, according to the techniques found in literature. Further analysis of the behaviour of the damage detection methods when there is noisy data or the damage in present in only one of the plies of the laminate is made, in order to test the resilience of the methods.

2.1 Laminated composite materials

Composite Materials consist of the combination of more than one type of material to obtain one which has desirable structural, electrical, or thermal characteristics, among others.

The topic of this thesis is that of Laminated Composite Materials, namely glass or carbon fiber reinforced polymers (GFRP and CFRP), which have been developed and studied for several decades. Structurally, the fibers contribute with a comparatively higher elasticity modulus in the longitudinal direction; and the polymeric matrix contributes to the structural integrity of the structure, distributing the loads among the fibers and acting as the medium in which the fibers are constrained.

The fiber materials are chosen, as mentioned before, for their high tensile strength. However, they are generally not rigid, and cannot form a rigid structure on their own, much like any other types of fibers. They are not considered to be isotropic, but actually orthotropic materials. The longitudinal elastic modulus is the main point of interest for the fibers, as this is the direction in which the fibers are strongest. In this direction, the fibers are the main contributor to the strength of the structure. In the transverse directions, the polymeric matrix is considered to be the main contributor to the structural

rigidity, which is about 13 times smaller than the longitudinal rigidity. This configuration results in an orthotropic composite material.

The denomination of Composite Laminates predicates the construction of laminae, which are composed by fibers aligned with one dimension - length -, a second dimension which has comparable size - width - and a third dimension with much smaller scale - thickness. Each lamina is assumed to have orthotropic properties, with the fiber direction being the principal one. There are other ways to make up a laminate, such as interwoven composite sheets or random distribution of short fibers, however this general case analysis represents a more versatile approach and is easily adapted to the alternatives.

To estimate the material properties for each lamina, assumptions about the material's behaviour must be made. It is assumed that the polymeric resin and the fibers have perfect cohesion, the matrix has no voids, there is a perfect (uniform) distribution of fibers, the applied loads are either perpendicular of parallel to the fiber direction and both the matrix and the fibers are isotropic and obey Hooke's law. This results in a state of isostrain which means that, for a given load, the fibers and the matrix will experience the same deformation. One of the main points of interest when developing a fibrous composite is the percentage of volume occupied by both the fibers and the matrix; the former is referred to as fiber volume fraction, represented as v_f. With these assumptions, we have the definitions made by Reddy [17] represented in Equation (2.1). The subscripts f and m correspond to the fibers and the matrix, respectively, and 1 and 2 correspond to the longitudinal and transverse directions of the lamina. The lamina's moduli (E and G) and Poisson's ratio (ν) are assembled in the compliance matrix $[S]$, as shown in Equation (2.2). The stiffness matrix $[C]$ is often employed as well, but with longer formulations of each member, and is the inverse of the compliance matrix ($[C] = [S]^{-1}$) for a stress-free initial state.

$$\begin{aligned} E_1 &= E_f v_f + E_m v_m; \quad & \nu_{12} &= \nu_{13} = v_f \nu_f + v_m \nu_m; \\ E_2 &= E_3 = \frac{E_f E_m}{E_f v_m + E_m v_f}; \quad & G_{12} &= G_{13} = \frac{G_f G_m}{G_f v_m + G_m v_f} \end{aligned} \tag{2.1}$$

$$[S] = \begin{bmatrix} \frac{1}{E_1} & \frac{-\nu_{21}}{E_2} & \frac{-\nu_{31}}{E_3} & 0 & 0 & 0 \\ \frac{-\nu_{12}}{E_1} & \frac{1}{E_2} & \frac{-\nu_{32}}{E_3} & 0 & 0 & 0 \\ \frac{-\nu_{13}}{E_1} & \frac{-\nu_{23}}{E_2} & \frac{1}{E_3} & 0 & 0 & 0 \\ 0 & 0 & 0 & \frac{1}{G_{23}} & 0 & 0 \\ 0 & 0 & 0 & 0 & \frac{1}{G_{13}} & 0 \\ 0 & 0 & 0 & 0 & 0 & \frac{1}{G_{12}} \end{bmatrix} \tag{2.2a}$$

$$\begin{Bmatrix} \varepsilon_1 \\ \varepsilon_2 \\ \varepsilon_3 \\ \varepsilon_4 \\ \varepsilon_5 \\ \varepsilon_6 \end{Bmatrix} = \begin{bmatrix} S_{11} & S_{12} & S_{13} & 0 & 0 & 0 \\ S_{21} & S_{22} & S_{23} & 0 & 0 & 0 \\ S_{31} & S_{32} & S_{33} & 0 & 0 & 0 \\ 0 & 0 & 0 & S_{44} & 0 & 0 \\ 0 & 0 & 0 & 0 & S_{55} & 0 \\ 0 & 0 & 0 & 0 & 0 & S_{66} \end{bmatrix} \begin{Bmatrix} \sigma_1 \\ \sigma_2 \\ \sigma_3 \\ \sigma_4 \\ \sigma_5 \\ \sigma_6 \end{Bmatrix} \tag{2.2b}$$

These equations are the results of the micromechanics approach, which is a theoretical base for

the computation of the ply's properties, and the assumptions made, which have more validity in some situations than others. There are different theoretical approaches, coupled with experimental validations of the results, which are outside of the scope of this thesis. When designing a laminated composite, it is often of interest that the material does not present a heavily orthotropic behaviour, which is the case for typical material properties for most fibers and resins used. This is the reason why several laminae are stacked in different orientations, to provide a more balanced material in the different directions, and which can be adjusted according to the application of interest. To couple the material properties of each lamina with a universal referential Oxy, the first step is to transform the lamina's properties with a transformation matrix, such as the one in Equation (2.3), where θ is the angle between the longitudinal direction of the lamina - 1 - and the x axis. The $[\bar{S}]$ and $[\bar{C}]$ matrices are the compliance and stiffness matrices in the universal referential.

$$[\bar{S}] = [R]^T[S][R] \tag{2.3a}$$

$$[R] = \begin{bmatrix} \cos^2(\theta) & \sin^2(\theta) & 0 & 0 & 0 & 2\sin(\theta)\cos(\theta) \\ \sin^2(\theta) & \cos^2(\theta) & 0 & 0 & 0 & -2\sin(\theta)\cos(\theta) \\ 0 & 0 & 1 & 0 & 0 & 0 \\ 0 & 0 & 0 & \cos(\theta) & -\sin(\theta) & 0 \\ 0 & 0 & 0 & \sin(\theta) & \cos(\theta) & 0 \\ -\sin(\theta)\cos(\theta) & \sin(\theta)\cos(\theta) & 0 & 0 & 0 & \cos^2(\theta) - \sin^2(\theta) \end{bmatrix} \tag{2.3b}$$

The previous equations are valid for all orthotropic materials, within the aforementioned assumptions. In the case of a laminated composite structure, an additional assumption of plane stress is made. This is due to the fact that the thickness of each lamina is usually much smaller that its length or width, so the transverse stress components are neglected. This generates the plane stress-reduced matrix $[Q]$. Its components are shown in Equation (2.4). It is essentially equivalent to removing the third through fifth rows and columns of the $[S]$ matrix and inverting it. The transformation to the universal referential is similar to the general case as well.

$$[Q] = \begin{bmatrix} \frac{E_1}{1-\nu_{12}\nu_{21}} & \frac{\nu_{12}E_2}{1-\nu_{12}\nu_{21}} & 0 \\ \frac{\nu_{12}E_2}{1-\nu_{12}\nu_{21}} & \frac{E_2}{1-\nu_{12}\nu_{21}} & 0 \\ 0 & 0 & G_{12} \end{bmatrix} \tag{2.4a}$$

$$\begin{Bmatrix} \sigma_1 \\ \sigma_2 \\ \sigma_3 \end{Bmatrix} = \begin{bmatrix} Q_{11} & Q_{12} & Q_{13} \\ Q_{12} & Q_{22} & Q_{23} \\ Q_{16} & Q_{26} & Q_{66} \end{bmatrix} \begin{Bmatrix} \varepsilon_1 \\ \varepsilon_2 \\ \varepsilon_3 \end{Bmatrix} \tag{2.4b}$$

$$[\bar{Q}] = [T]^T[Q][T] \tag{2.4c}$$

$$[T] = \begin{bmatrix} \cos^2(\theta) & \sin^2(\theta) & \cos(\theta)\sin(\theta) \\ \sin^2(\theta) & \cos^2(\theta) & -\cos(\theta)\sin(\theta) \\ -2\cos(\theta)\sin(\theta) & 2\cos(\theta)\sin(\theta) & \cos^2(\theta) - \sin^2(\theta) \end{bmatrix} \tag{2.4d}$$

In order to integrate the several laminae in the composite's material model, a vertical coordinate must be used, to account for the different laminae's behaviour when not in plane stress. Considering a laminated plate with total thickness h with N layers, and with the referential centered in the mid-point of the plate thickness. The k^{th} layer is located between the points $z = z_k$ and $z = z_{k+1}$, as shown in Figure 2.1.

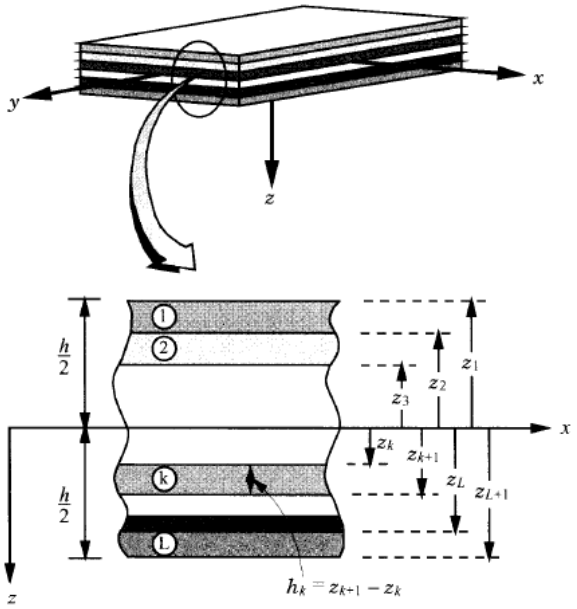

Figure 2.1: Layers numbering system and coordinates [17]

The laminate's properties can then be computed for bending and extensional loads with the laminae's $[\bar{Q}]$ matrices and the z coordinates. These properties are assembled in three matrices, $[A]$, $[B]$ and $[D]$, which are called the extensional stiffness matrix, bending stiffness matrix and bending-extensional coupling stiffness matrix respectively. The formulas used to calculate the value of each element can be found in Equation (2.5).

$$\begin{aligned} A_{ij} &= \textstyle\sum_{k=1}^{N} \bar{Q}_{ij}^{(k)} (z_{k+1} - z_k), \\ B_{ij} &= \textstyle\sum_{k=1}^{N} \bar{Q}_{ij}^{(k)} \frac{(z_{k+1}^2 - z_k^2)}{2}, \\ D_{ij} &= \textstyle\sum_{k=1}^{N} \bar{Q}_{ij}^{(k)} \frac{(z_{k+1}^3 - z_k^3)}{3} \end{aligned} \tag{2.5}$$

The quantities used to express the loads acting on the laminate are called in-plane force resultants, N_{xx}, N_{yy} and N_{xy}, and moment resultants, M_{xx}, M_{yy} and M_{xy}. They are the results of the integration of the stresses in the same planes through the thickness of the plate. The resultant relation can be seen on Equation (2.6). By finding the inverse of the $[A]$ matrix, we can also find the laminate's modules and

Poisson's coefficient.

$$\begin{Bmatrix} N_{xx} \\ N_{yy} \\ N_{xy} \\ M_{xx} \\ M_{yy} \\ M_{xy} \end{Bmatrix} = \begin{bmatrix} A_{11} & A_{12} & A_{16} & B_{11} & B_{12} & B_{16} \\ A_{12} & A_{22} & A_{26} & B_{12} & B_{22} & B_{26} \\ A_{16} & A_{26} & A_{66} & B_{16} & B_{26} & B_{66} \\ B_{11} & B_{12} & B_{16} & D_{11} & D_{12} & D_{16} \\ B_{12} & B_{22} & B_{26} & D_{12} & D_{22} & D_{26} \\ B_{16} & B_{26} & B_{66} & D_{16} & D_{26} & D_{66} \end{bmatrix} \begin{Bmatrix} \varepsilon_{0x} \\ \varepsilon_{0y} \\ \gamma_{0xy} \\ -\frac{\partial^2 w_0}{\partial x^2} \\ -\frac{\partial^2 w_0}{\partial y^2} \\ -2\frac{\partial^2 w_0}{\partial x \partial y} \end{Bmatrix} \tag{2.6a}$$

$$\begin{cases} \varepsilon_x = \varepsilon_{0x} - z \cdot \frac{\partial^2 w_0}{\partial x^2} \\ \varepsilon_y = \varepsilon_{0y} - z \cdot \frac{\partial^2 w_0}{\partial y^2} \\ \lambda_y = \lambda_{0xy} - z \cdot 2\frac{\partial^2 w_0}{\partial x \partial y} \end{cases} \tag{2.6b}$$

$$h[A]^{-1} = \begin{bmatrix} \frac{1}{E_x} & -\frac{\nu_{yx}}{E_y} & 0 \\ -\frac{\nu_{xy}}{E_x} & \frac{1}{E_y} & 0 \\ 0 & 0 & \frac{1}{G_{xy}} \end{bmatrix} \tag{2.6c}$$

A laminate's stacking, or lay-up, nomenclature has specific rules. By default, all of the plies are considered to have the same thickness and be the same material. The order of the orientations is presented between parentheses, from bottom to top, and the orientations of the plies (between $-90°$ and $90°$) are separated by a forward slash and in degrees. If there is a sequence of plies with the same orientation, the number of repetitions can be used in subscript; if the lay-up is symmetric, only half of the lay-up is written and a subscript s is used outside the parentheses; and if there are different thickness plies but the thicknesses are multiples of each other, this can be reflected in the repetitions.

The stiffness elements A_{ij} have no dependence of the z coordinate, as it pertains to plane stress, and it only depends on the stiffness and thickness of the laminae. However, the bending stiffness elements D_{ij} are proportional to the z coordinate; this means that the choice for the placement of each layer will only affect the bending deformation under a given load. Considering two different lay-ups, $(0/90)_s$ and $(90/0)_s$, both will have the same in-plane stiffness and the values of A_{ij} will be the same for both; but in bending, the first will be more rigid in the x direction (i.e. a moment around y), as the plies with 0° orientation (which are stiffer in the x direction) are closer to the outside; the values for D_{ij} for both of these lay-ups will then be different.

A symmetric laminate will have all members of the $[B]$ matrix as zero. This option provides a more stable reaction to thermal variations, as it will not have a tendency to twist when different layers contract or expand unbalanced. On the other hand, unsymmetrical lay-ups may be of interest if the application requires unsymmetrical force, construction or thermal loads.

2.2 Natural frequencies and mode shapes

The proposed analysis of composite structures is based on the study of their respective mode shapes, which are obtained experimentally or numerically and correspond to a dynamic analysis of the structure.

Mode shapes are essentially the geometric patterns which bodies assume when excited to specific frequencies, called modal or natural frequencies. The value of the frequencies and the shapes are characteristic of the specific geometry and material properties of the object of study. A comprehensive review of the historical landmarks in this area of study and different analytical methods used to determine these shapes and frequencies can be found in *Mechanical Vibrations*, by Rao [18]. For an undamped system, the free vibration is given by the formula in Equation (2.7)

$$\Big[M\Big]\Big\{\ddot{\Delta}\Big\} + \Big[K\Big]\Big\{\Delta\Big\} = 0 \tag{2.7}$$

Where $[M]$ is the Mass matrix, $[K]$ is the stiffness matrix, $\{\Delta\}$ is the displacement vector, and $\Big\{\ddot{\Delta}\Big\}$ is its second order derivative with respect to time. If the structures' behaviour is linear, the response is harmonic and has the form shown in Equation (2.8)

$$\Big\{\Delta\Big\} = \Big\{\phi_q\Big\}\, cos(\omega_q t) \tag{2.8}$$

Where ϕ_q is the eigenvector or mode shape and ω_q is the natural angular frequency for mode q. This solution is then replaced in Equation (2.7) and yields Equation (2.9), which is an eigenvalue problem. For this type of problem, especially on complex cases, a Finite Element software is employed.

$$\left([K] - \omega^2\,[M]\right)\{\phi_q\} = 0 \tag{2.9}$$

When comparing two similar structures, the least rigid is expected to have lower natural frequencies for each mode. Having this in mind, the first step in comparing damaged and undamaged composite plates is to compare the values of the natural frequencies, as the damaged plate will be less rigid and thus have lower natural frequencies. However, the differences in the values of the frequencies are often very small, well within the margin for experimental noise, especially for a light Damage Case, as the literature suggests [6]. Moreover, this method alone has not yet been used for determining the location of the damage. To mitigate these shortcomings, the mode shape analysis may be of help.

The analysis of mode shapes allows to locate and possibly quantify damage in these composite plates, with differing degrees of resolution or precision depending on the quality of the data sampling. The first step is to analyse the displacement of the plate when excited to a natural frequency. Then, the displacement field is post-processed in order to obtain spatial derivatives. In this thesis, the Finite Difference Method is used to compute the rotations (first derivative), curvatures (second derivative) and higher order derivatives. This process is better analysed in Sections 2.5 and 2.6.

2.3 Finite Element Method

The computational modelling of the plate is made using the Finite Element Method (FEM). This method consists of dividing the complex domain in which the simulation takes place into simple subdomains, called Finite Elements (FE). For a complex simulation, an analytical solution is not always viable or even existent. However, in each of the elements, if they are correctly defined, a numerical solution can be achieved, using their material and geometric properties in conjunction with the appropriate laws. Then, by assembling all the finite elements and defining the boundary conditions, a coherent solution for the entire domain can be found. The FEM can be used to solve problems in structural, thermal or electrical analyses, among others, but in this case only the former is of interest and thus will be further analysed.

For the case at hand, the simulations carried out are of rectangular laminate composite plates. Usually, for the undamaged plates, analytical solutions can be found for the natural frequencies and mode shapes. However for the damaged ones, this is often not possible and the FEM is the method used to compute these solutions.

According to Reddy [19], there are essentially three steps to solve a FE analysis:

1. Dividing the domain in a mesh of finite elements, including the generation of the geometric properties
2. Generation and derivation of the element equations
3. Assembly of the elements

For the first step, there are several types of elements, which should be selected according to the intended purpose. The first criteria to consider is the number of dimensions the elements have. There are 1D elements usually used for beams, 2D elements usually used for plates and shells, and 3D elements which are used in solids. With each additional dimension come subsequent variables to consider, such as element shape, dimensions and larger computational processing; for instance, a 2D element can be a triangle or a rectangle while a 1D element can only be a straight line. Thus, for simplicity, more effective troubleshooting of the solutions and faster computation, the element of choice for each application should be of the smallest number of dimensions. For the subject at hand in this thesis - thin composite plates -, 2D elements are used. The choice of the 2D type is based on the fact that one of the dimensions (thickness) is much smaller than the other two (length and width). The physical properties of the composite laminate can be inserted in the FE software to compute the plate properties. For 2D elements, either triangles or rectangles can be used; in this case, the choice was for rectangles, as it allows for a better implementation on the Finite Differences Method with uniform meshing.

Another variable to consider is the number of degrees of freedom per node. Nodes are points which are associated to each element and the connection of adjacent elements, and can be found either at the border or the interior of the elements. These points are the ones where the solution of the equations is computed. There is a maximum of six degrees of freedom that each node can have: three for translation and three for rotation, one of each for each axis. The type of element has this choice implied, according

to the pertinence of the assumptions made for each element type, and should encompass the most relevant degrees of freedom for the intended solution.

The second step refers to the use of approximation functions in the FEM. These are selected in order to meet the requirements of the boundary conditions on each node. This process, along with the third step, is developed autonomously by the FEM software of choice, and its success is a result of the choices made in the first step. For a further in-depth analysis of the equations and mathematical formulations behind the Finite Element Method, an interested reader could consult the comprehensive analysis made by Reddy [19]; as the use of the FEM in this thesis is only through the use of a specific software and these operations are not worked on directly, this analysis is then considered to be outside the scope of this thesis.

2.4 Damage Models

For the FE model, an important choice is how to simulate the damage in the composite plates. In this section, three different approaches from different authors are presented. These approaches are defined according to the initial analysis made by the authors, regarding the physical meaning of each assumption. The strong and weak points of each approach are also discussed. As no experimental trials are performed in the context of this thesis, the study of the physical significance of each model is only made in comparison with other numerical results.

2.4.1 Microphenomenology

This Damage Model was proposed by Ladevèze and Lubineau [20] in the article *On a damage mesomodel for laminates: micromechanics basis and improvement*. In the original paper, the physical phenomena regarding the matrix and matrix-fiber interface are explored on the micro scale to create damage mesomodels, which correspond to damage parameters. The elastic constants of the damaged case are presented in Equation (2.10).

$$\begin{cases} \widetilde{E}_1 = E_1 \\ \widetilde{E}_2 = E_2 * (1 - d') \\ \widetilde{G}_{12} = G_{12} * (1 - d) \end{cases} \quad \text{with } 0 \leq d, d' \leq 1 \tag{2.10}$$

This model was developed by the authors using FE simulation data and previous experimental results, and it predicts the presence of transverse microcracking in the matrix, as well as fiber/matrix debonding. On the longitudinal direction of the fibers (i.e. E_1), it is assumed that there is no plastic deformation, given the comparatively higher yield stress of the fibers. In the transverse direction (i.e. E_2), the damage in the matrix is characterized by the variable d', denominated as transverse damage parameter. For the shear modulus G_{12}, it is considered that the shear damage parameter d is the same for both compression and traction. Each of these two damage parameters may have values between 0

and 1, where a value of zero is equivalent to no damage at all, and a value of 1 is a complete loss of stiffness in the corresponding direction.

The authors predict two damage modes: Mode 1, where there is diffuse damage, fiber-matrix debonding and a loss of shear stiffness; and Mode 2, where there is matrix microcracking through the ply thickness and a loss of tenacity in the matrix[1]. Mode 1 is considered to be superseded by Mode 2 when both phenomena are occurring. One of the main variables of interest is the cracking rate ($1/\rho = H/L$, where H is the ply thickness and L is the spacing between cracks), and it serves as an independent variable to the damage parameters. There are damage parameters associated with Mode 1 ($\tilde{d}$ and $\tilde{d}'$), which are not dependant on the cracking rate; it is considered that the transverse damage parameter is dependant on the shear damage parameter by the law $\tilde{d}' = b_3 * \tilde{d}$, where b_3 is a characteristic of the material. The damage parameters associated with Mode 2 ($\bar{d}$ and $\bar{d}'$) are dependant on the cracking rate. When Modes 1 and 2 are superimposed, the damage parameters to consider are the ones from Mode 2 ($\bar{d}$ and $\bar{d}'$), which are now dependant on $1/\rho$ and $\tilde{d}$. The damage parameters in Equation (2.10) are substituted by the relevant ones, according to the Damage Mode being analysed.

The damage parameters associated with each damage mode (i.e. with a tilde or bar) are the result of the microscale considerations being made, regarding the interior of the ply. Equation (2.10) refers to the mesomodel of the ply at study, where the microscale parameters are chosen according to what is shown in Table 2.1.

	Mode 1	Mode 2
Microscale Parameters	$\tilde{d}$, $\tilde{d}'$	$\bar{d}$, $\bar{d}'$
Damage Mode present	Microscale Parameters used	
1	X	
2		X
1+2		X

Table 2.1: Damage Parameters use in the Microphenomenology damage model

This damage model is relatively complicated to use, as it has several different variables to manipulate while creating simulations, which may lead to a large number of tests to evaluate the different variables. The results of this model may however be closer to what is expected when comparing with experimental results, since it has a high level of adjustability. The fact that the resulting elasticity constants vary on whether the material is in compression or in traction, while physically sound, may not be possible to account for while simulating this model in a FE software, as will be seen on Chapter 3.

2.4.2 Reduction of the Laminated Stiffness

A damage modelling approach proposed by Moreno-García et al. [8] - RLS - considers only a single damage variable, $d^{(e)}$, denominated elemental damage parameter, as the superscript (e) is in reference to the loss of stiffness of each of the affected elements, as shown in Equation (2.11).

[1] Note: in the original paper, Modes 1 and 2 are referred to as Scenarios 3 and 1, respectively

$$\left\|[\tilde{D}_{(e)}]\right\| = (1 - d^{(e)}) * \left\|[D_{(e)}]\right\| \tag{2.11}$$

$$\text{with } 0 \leq d_{(e)} \leq 1$$

In this case, the $[D]$ matrix is used in reference to the laminate stiffness matrix, such as shown in Section 2.1. Performing this operation is equivalent to multiplying the elastic constants of the laminate by the damage parameter, as all non-zero terms of the stiffness matrix are proportional to the elastic constants of the laminate. As the laminate stiffness is proportional to the individual plies' elastic constants, these terms can then be expressed as in Equation (2.12).

$$\begin{cases} \tilde{E}_1 = E_1 * (1 - d^{(e)}) \\ \tilde{E}_2 = E_2 * (1 - d^{(e)}) \\ \tilde{G}_{12} = G_{12} * (1 - d^{(e)}) \end{cases} \tag{2.12}$$

$$\text{with } 0 \leq d_{(e)} \leq 1$$

Just as in the model in Section 2.4.1, a value of zero in the damage parameter $d^{(e)}$ is equivalent to no damage at all, and a value of 1 means a complete loss of rigidity in all directions. This model, as it only has one variable, is much simpler to implement than the one on Section 2.4.1. However, it may not be as close to reality, if compared to experimental results. Its simplicity is nevertheless advantageous when testing the sensibility of the damage detection methods to low damage parameters.

2.4.3 Teflon® tape inclusion

This method is commonly used in experimental setups to create a controlled case of delamination. This consists of the inclusion of a piece of Teflon® tape inside the laminate while laying the composite plies, usually in the mid-plane of the laminate.

The use of Teflon® is motivated by the fact that the epoxy resin does not bond to this material. The inclusion of this piece of tape will then lead to the adjoining layers not bonding, and thus to a delamination case. The elastic constants of Teflon® are much smaller than those of a CFRP ou GFRP lamina (about two orders of magnitude [21]), which is why it is safe to assume that the tape has no contribution to the strength of the plate, while ensuring that no further damage is made to the composite material.

As this is a notable example of experimental controlled damage simulation, its inclusion in the simulations array is important. The implementation of this case in the simulations is made using the Modelling of the elementary ply method with high values in the damage variable associated with delamination d and low values in the others, as there are no other practical and physically sound alternative implementations.

2.5 Finite Difference Method

All the damage detection methods chosen use spatial derivatives of the displacement fields to obtain rotations, curvatures, and higher order derivatives. The Finite Difference Method was then the method chosen to numerically calculate these derivatives. It should be noted that experimental techniques only allow the measuring of the mode shapes and modal rotations [22]; this justifies the need to apply numerical differentiation techniques to experimental data to obtain the modal curvature and higher order derivatives. The basis for this method is a commonly used approximation of a continuous function derivative, as shown in Equation (2.13).

$$f'(x)_{forward} = \lim_{h \to 0} \frac{f(x+h) - f(x)}{h} \tag{2.13}$$

The example shown is that of a forward finite difference with an element size h tending to zero. The central finite difference seen in Equation (2.14) was preferred in the work described in this thesis, as it is, in most cases, more precise than the forward and backward differences, especially for the computation of higher order derivatives. The formulae for the derivatives calculated from the Finite Difference Method are found in Equations 2.14-2.17. These are calculated using the first derivative formula (2.14) and applying it to itself successively - i.e. $\frac{\partial^2 w}{\partial x^2} = \frac{\partial}{\partial x}(\frac{\partial w}{\partial x})$. These formulas and the corresponding analysis can also be found in [23].

$$\frac{\partial w}{\partial x} = \frac{-\frac{1}{2}w(x-h,y) + \frac{1}{2}w(x+h,y)}{h} \tag{2.14}$$

$$\frac{\partial^2 w}{\partial x^2} = \frac{w(x-h,y) - 2w(x,y) + w(x+h,y)}{h^2} \tag{2.15}$$

$$\frac{\partial^3 w}{\partial x^3} = \frac{-\frac{1}{2}w(x-2h,y) + w(x-h,y) - w(x+h,y) + \frac{1}{2}w(x+2h,y)}{h^3} \tag{2.16}$$

$$\frac{\partial^4 w}{\partial x^4} = \frac{w(x-2h,y) - 4w(x-h,y) + 6w(x,y) - 4w(x+h,y) + w(x+2h,y)}{h^4} \tag{2.17}$$

This method has inherent sources of error, as it is a numerical approximation of the differentiation of the mode shapes. The error of the differentiation on the n^{th} derivative is proportional to h^n. This means that, in order to minimize error, a balance should be found between a small enough element size to obtain an accurate differentiation, and not too small where the rounding errors of the results and noise in the data compromise the solution.

2.6 Damage indices

The damage indices introduced in this section are the methods used to detect and localize damage. These are numerical tools applied in the post-processing of the modal displacements results; they produce a real and positive value for each node of the plate. Analysing the complete field of values, one can find the nodes at which they are highest, and those should correspond to the damaged areas. The accuracy of this correspondence dictates the quality of the damage detection. The first two were

proposed and used by previous authors and the third is being proposed in this work.

2.6.1 Difference in Field Derivatives

This Damage index - Difference of Field Derivatives (DFD) - was proposed by Moreno-García et al. [8], and it compares spatial derivatives in one direction, using different degrees of derivation, between the damaged and undamaged plates' mode shapes, as shown in Equation (2.18). The q index refers to the mode shape being analysed, and this method is used up to the fourth derivative ($P = 1, 2, 3, 4$).

$$DFD_q^{(P)}(x,y) = \left| \frac{\partial^P w_q(x,y)}{\partial x^P} - \frac{\partial^P \tilde{w}_q(x,y)}{\partial x^P} \right| \tag{2.18}$$

The derivatives are calculated using the Finite Difference method, with the formulas from Equation (2.17).

This method analyses each mode separately, which can be useful when the damaged area is on points of the mode shape with especially high or low values of displacement. The higher degrees of derivation, although seemingly more sensitive to damage, may also be more susceptible to inaccuracies or noise. The fact that the derivatives are calculated along only one direction - x -, may also be of note when analysing the results.

2.6.2 Translation, Slope, and Curvature Differences

A second damage detection method was proposed by Araújo dos Santos et al. [6] - TD, SD and CD -, and it uses an euclidean vector approach to the derivative analysis of the mode shapes, as well as the sum of the results of several modes to detect damage, as seen on Equation (2.19).

$$TD(x,y) = \frac{1}{n} \sum_{q=1}^{n} |w_q(x,y) - \tilde{w}_q(x,y)| \tag{2.19a}$$

$$SD(x,y) = \frac{1}{n} \sum_{q=1}^{n} \left| \|\boldsymbol{\theta}_q(x,y)\|_2 - \left\|\tilde{\boldsymbol{\theta}}_q(x,y)\right\|_2 \right| \tag{2.19b}$$

$$CD(x,y) = \frac{1}{n} \sum_{q=1}^{n} \left| \|\boldsymbol{\kappa}_q(x,y)\|_2 - \|\tilde{\boldsymbol{\kappa}}_q(x,y)\|_2 \right| \tag{2.19c}$$

This method uses all components of the rotation and curvature vectors at each node to calculate their respective magnitude; it is the magnitude of these vectors that is then compared between the damaged and undamaged plates. The components of these vectors are laid out in Equation (2.20).

$$\boldsymbol{\theta}_q(x,y) = \begin{Bmatrix} (\theta_x)_q(x,y) \\ (\theta_y)_q(x,y) \end{Bmatrix} = \begin{Bmatrix} \dfrac{\partial w_q(x,y)}{\partial x} \\ \dfrac{\partial w_q(x,y)}{\partial y} \end{Bmatrix} \tag{2.20a}$$

$$\boldsymbol{\kappa}_q(x,y) = \left\{ \begin{array}{c} \dfrac{-\partial^2 w_q(x,y)}{\partial x^2} \\ \dfrac{-\partial^2 w_q(x,y)}{\partial y^2} \\ -2\dfrac{\partial^2 w_q(x,y)}{\partial x \partial y} \end{array} \right\} \tag{2.20b}$$

Just as in Section 2.6.1, the Finite Difference method is used to calculate the derivatives.

Comparing with the DFD method, very different choices are made regarding several aspects of the damage detection. The three main differences are that several modes are compared at once, only two degrees of derivation are used and the difference is calculated from the euclidean norms of the vector corresponding to each degree of derivation. The relative predicted advantages and disadvantages of this method are then the inverse of the ones stated on the end of Section 2.6.1.

2.6.3 Sum of Field Derivatives

This damage index - SFD - is being proposed as a means to evaluate the performance of the choices made in the previous two, and it consists essentially of a mix of both. The derivation is computed in one direction only and up to the fourth degree, as in the DFD method; then the results of several modes are averaged as in the TD, SD and CD method. The formula for this damage indicator is shown in Equation (2.21).

$$SFD^{(P)}(x,y) = \left| \frac{1}{n} \sum_{q=1}^{n} \left(\frac{\partial^P w_q(x,y)}{\partial x^P} \right) - \frac{1}{n} \sum_{q=1}^{n} \left(\frac{\partial^P \tilde{w}_q(x,y)}{\partial x^P} \right) \right| \tag{2.21}$$

This approach serves the purpose of testing both the derivation approaches and the single/multiple mode analysis. One important factor that this approach might help analyze is the relation between the damage localization and specific mode shapes, where it might hinder or improve damage detection.

Chapter 3

Implementation

The Damage Detection Methods described in Chapter 2 are applied to data gathered through the development of FE models of the plates with and without damage. Different modal analyses are conducted, namely for clamped and free plates, so that different modes of vibration can be studied. To account for a possible source of experimental uncertainty, artificial noise is generated and added to the simulation results, so that the damage detection methods can be tested in a data set that more closely resembles a real world environment.

The complete source code developed and used for the work described in this thesis can be found on MATLAB Central File Exchange[24].

3.1 Finite Element Model

3.1.1 APDL® algorithm

The FE simulations are run using Ansys®, though a Mechanical APDL® script.

Ansys® Parametric Design Language (APDL®) is a language which sends instructions to the FE software. This allows the modelling and simulation of a given problem, through specific commands, with an input file. It is also possible to run this input file by launching the program through a Matlab® script. This method is highly advantageous to the task at hand, as it can be used to run the simulation and extract all the necessary results within the Matlab® environment, after manipulating the variables as desired, to correspond to the different cases as they are being developed and studied.

Each step of the process is documented in Figure 3.1. The way this is accomplished for each different case is through the Matlab® function *edit_log.m*. The values of interest are substituted into the input file, according to the order of operations described in the flowchart in Figure 3.1. The input file also contains instructions to print the nodal coordinates, nodal displacement results and natural frequencies to text files. These can in turn be imported to Matlab® to be post-processed once the simulation reaches its end.

The various steps are divided in sections, namely Preprocessor, Solution and Post-processor. Each possible instruction in the APDL® is associated with a specific section, and can't be used outside of this

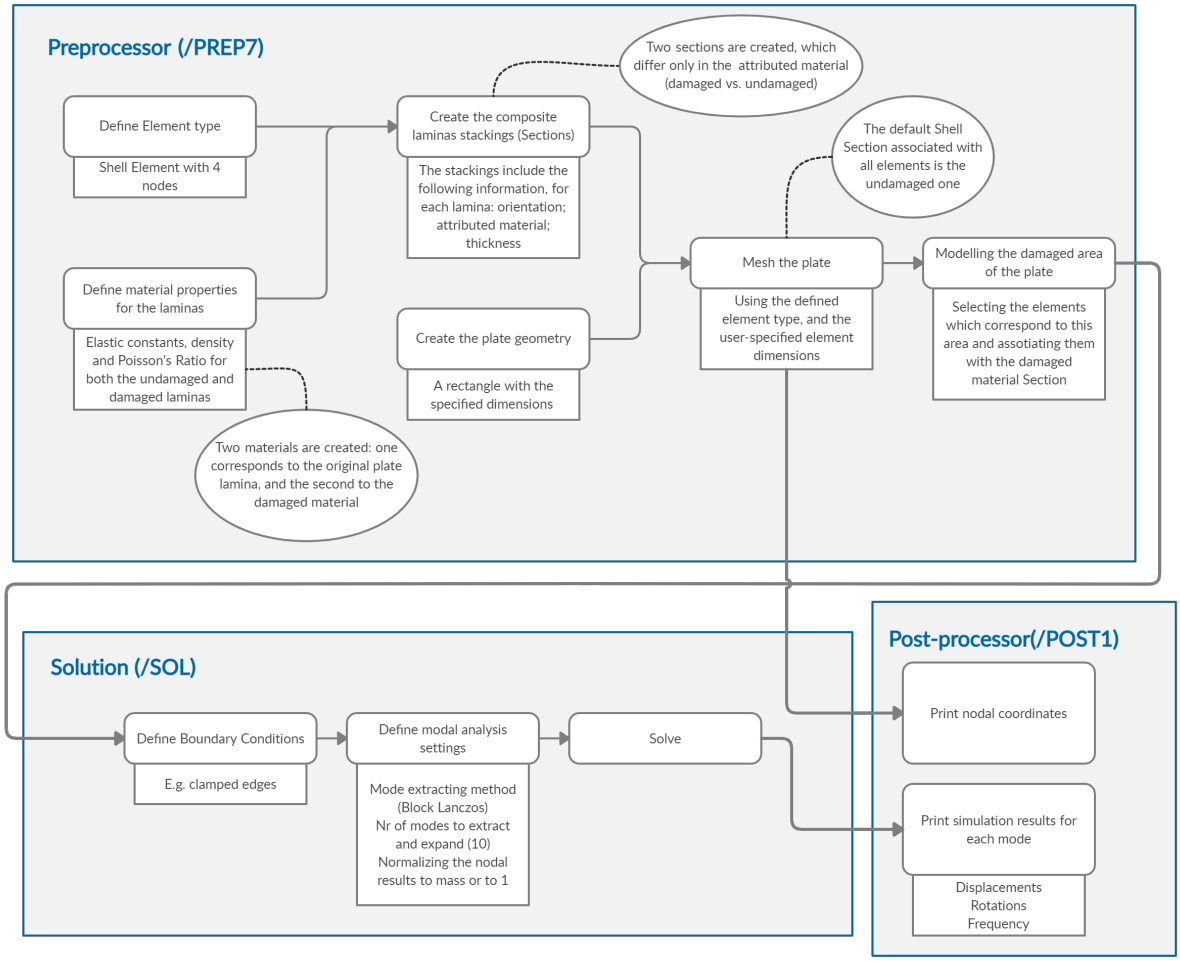

Figure 3.1: Flowchart describing the APDL® modelling process

context. Each section is opened with a command (/PREP7 for the pre-processor, for example) and it is only considered as closed when another section is opened.

Preprocessor

In the Preprocessor, the model is established. It includes the material information, the geometric characteristics and the FE mesh.

The material is defined by the lamina's properties; the used values are for pre-made laminae, and as such the uncertainties associated with the micromechanics approach are mitigated. The Element type is chosen; the *Shell181* element was chosen for being a rectangular shell element with four nodes and six degrees of freedom per node: three for displacement and three for rotation; no other element types were comprehensively tested, as this one satisfied the required criteria and the number of variables being studied is considered to be sufficient. Another material model is created, with the damaged material's properties assigned to it.The laminate stacking is made with the *Sections* control, which associates to the element type a material information; this information is the result of the combination of the several laminae - with their respective thicknesses and orientations - and composes the laminate's stiffness

matrix. Once again, a second section is created, with the associated material being the one that has the damage case properties.

The following step is to generate the geometry, which is a rectangle with the plate's in-plane dimensions (length and width). Given that the chosen element type is a shell element, a 2D figure is all that is needed.

The FE mesh is created on the plate, with two previously defined inputs: the element type (which includes the material information) and the desired element dimension. The element dimension should be a whole division of the plate's dimensions, so that the mesh is square and uniform. In the simulations in which a damaged plate is modelled, there is one additional step in the Preprocessor stage: the elements which are considered to be in the damaged area are selected, and their associated section is changed to the damaged one.

Solution

In this section, the Solution options are made, regarding the modal analysis and simulation.

The simulations made have one of two boundary conditions: either all edges of the plate are clamped, or the plate is free in space. On the latter case, the first six modes are the results of translation or rotation on each of the six degrees of freedom, and as such are discarded.

The modal analysis has several variables. First, the number of modes to be extracted is defined as ten, as it seems to be a good compromise between the volume of the data set, the needed computational resources and the ability to analyse the information, as well as the case in the literature which features the same choice [6]. The chosen extracted method is Block Lanczos, which is the default and most commonly used in the Ansys® environment, and as such should be the most stable for this application; no other extraction methods were comprehensively tested.

The last step in the Solution section is to solve the problem, i.e. to calculate the simulation results.

Post-processor

In the Post-processor section, all of the instructions to output the desired information are given. The outputs are exported as text files. For the nodal data, the nodes are numbered, which allows the direct indexation of the different data points - coordinates and displacements.

The nodal coordinates are extracted directly from the initially established FE model. The simulation results of interest are the natural frequencies - which are printed as a list - and the nodal displacements - which are printed as nodal data.

3.1.2 Damage Simulation

The damage simulation is made by changing the elastic constants of the elements which are considered to be damaged.

As stated in Section 3.1.1, when creating the material properties, two different materials are defined: one which has the original lamina's properties, and another with the damaged one's, which are in turn

associated with their respective elements. In the damage cases, as described in Section 2.4.1 and 2.4.2, the damaged elements' constants are a result of multiplying the original constants by a specific coefficient; as in the APDL® algorithm each constant is defined individually, either one of the damage mechanics models is implemented in the same way.

3.2 Results post-processing

The results of the simulation are exported from Ansys® to text files, and they are then imported into a Matlab® script and processed in the form of matrices with double precision.

To account for the possibility that the mode shapes have flipped directions between simulations, a dot product is calculated between the displacement vectors of the damaged and undamaged plates, in each post-processing routine. If this dot product is positive, the mode shapes are both in the same direction; however if it is negative, is means that they are of opposite signals, and its displacement field is inverted by multiplying all values by -1.

For each case's nodal displacements, the different derivation operations and damage indices, figures are generated, using Matlab® graphics tools. For the damage indices, *Scatterbar3* [25] is used, to better visualise the more isolated nodal values, and for the displacement and derivative fields *Trisurf* is used, to better visualise the continuous field of values.

3.2.1 Finite Differences

Using the formulas from Equation (2.17), each each of the derivative orders is computed according to their respective formulas. The matrices have the following nodal information in each column: 1. Node index; 2. X coordinate; 3. Y coordinate; 4. Transverse displacement.

The following algorithm is referent to the calculation of a derivative in the X direction. To calculate in the Y direction, the same algorithm is used, switching columns 2 and 3. The nodes are ordered by their respective indices, which may or may not correspond to them being ordered by one of the coordinates. For this reason, the lines of the matrix are then ordered by the values in the third column, and secondarily by the second column. This results in an order which represents the nodes by rows in the Y direction and, for each row, are ordered by their X coordinate. In this assortment, the derivation in X is made line-by-line.

For the first and second derivatives, the first and last nodes of each row are ignored, as the second order central finite difference needs one node on either side to be calculated; for the third and fourth derivatives, two nodes on either side are used, so the first and last two nodes are ignored and are left with a NaN value.

To calculate the derivative in each node, the displacement values of the nodes of interest (the node at which the finite difference is being calculated and neighbouring nodes) are multiplied by their respective coefficients, and their sum is divided by the spacing between the points. To account for spacing variations, the spacing is calculated using the values in column 2 for each node, instead of using the

same value for all nodes. When the end of the row is reached, the same process is restarted for the following row, until all the nodes of the plate are processed.

This method is valid for all derivative orders and is also used to perform the needed cross partial derivatives (e.g. $\frac{\partial^2 w}{\partial x \partial y} = \frac{\partial}{\partial y}(\frac{\partial w}{\partial x})$), by performing the operation on the result of a previous derivation.

3.2.2 Noise simulation

In order to simulate this aspect of experimental conditions, noise is generated and added to the displacement results obtained by the FE simulations.

The noise generation is a normal distribution of random numbers with a standard deviation of 10^{-6} and an average of zero, and with the same matrix size as the displacements data set. This noise intensity is very small, as the displacements are normalized to 1, and as such it is about six orders of magnitude smaller. To simulate larger noise volumes, a Noise Level (NL) is used to multiply the generated noise, from 1 (barely noticeable) up until the results are severely compromised; this maximum value is explored in each case.

To obtain statistically valid results, i.e. so that a possible imbalance in the randomly generated noise does not skew the results, a battery of 200 post-processing routines is run, where in each routine a new random noise field is generated. The noise is only added to the displacement field of the damaged plate simulation, to mimic a situation where only the damaged plate is experimentally tested. Equation (3.1) shows the basic algorithm for the noise generation and addition, where *normrnd* is a Matlab® function which generates random numbers in a normal distribution, as intended.

$$noise(x,y) = normrnd(average, std\_dev, matrixsize), average = 0, std\_dev = 10^{-6} \tag{3.1a}$$

$$\tilde{w}_{q,NL}(x,y) = \tilde{w}_q(x,y) + NL * noise(x,y) \tag{3.1b}$$

The more commonly emplyed measure of Signal-to-noise ratio (SNR) is not directly employed, however given that the displacement results are normalized and the noise follows a normal distribution with a predetermined standard deviation, it can easily by calculated by multiplying the Noise Level by 10^6 (i.e. $SNR = NL * 10^6$); for instance, a Noise Level of 10000 corresponds to $SNR = 100:1$ or 20 dB.

3.2.3 Results quality index

So that the different damage detection methods, as well as different application of each method, can be compared quantitatively, an evaluator μ_q proposed by Moreno-García et al. [26] is used for each analysis, defined in Equation (3.2).

$$\mu = 1 - \frac{1}{NN}\sum_{k=1}^{NN} \widehat{DI}(x,y)\ ,\ \widehat{DI}(x,y) \leq 1 \tag{3.2}$$

NN is the number of nodes, and the hat denotes that the damage indicator is normalized, i.e. its maximum nodal value is 1. DI is used to represent the nodal value of any damage index that is chosen to apply this method.

The maximum value that this quality index can assume is 1, which corresponds to a single node at which the damage indicator is 1 and all of the other nodes with the indicator at zero; this should correspond to a perfect damage detection, if the peak value is located at the damaged area. On the contrary, a quality index of zero corresponds to a field of all equal values, which naturally does not allow the identification of damage.

This quality index has the important role of quantifying the results' behaviour, however its shortcomings should be taken into account. It doesn't account for the possibility of multiple damaged areas, and it does not discriminate situations where the damage is correctly identified from situations where peaks emerge for other reasons, such as mathematical instability. For these reasons, this index is always used in context with different analyses and accompanied by a qualitative analysis of the results in figures.

3.3 Simulation and analysis data

With the different variables at play, this section serves the purpose of listing the different simulations to be run, as well as the post-processing analysis for each. The main variables to test individually are:

1. Plate properties
2. FE model element size
3. Damage mechanics and parameters for the simulations
4. Damage indicators and derivative orders for the damage detection
5. The relation between the damaged area location and the mode shapes, regarding damage detection
6. Different noise levels

3.3.1 Plate properties

Table 3.1 lists the properties that characterize the plate used in the simulations, as well as some simulation choices made. The laminate stacking is used by Ladevèze and Lubineau [20] to determine the damage parameters, the dimensions are used by Moreno-García et al. [8] in a similar study, where the DFD method is employed, and the material properties are typical for this material with 60% fiber volume [27].

3.3.2 Element sizing in the FE simulations

The element sizing, namely the distance between nodes, has an effect on mainly three parts of the analysis: computation time (a finer mesh has more nodes and thus take longer to simulate and

Stacking sequence	$(90/0_2)_s$		
Material	AS4/3501-6 Carbon-epoxy		b_3=0.5
Density (kg/m^3)	1550		
Dimensions (mm) Length |Width |Thickness	400	200	0.75
Elastic Constants (GPa) E_1 |E_2 |G_{12}	138	10.3	6.9
Poisson's Ratio ν_{12}	0.3		
Boundary conditions	Free in space	Clamped edges	
Damage Scenario	Center	Corner	Center + Corner

Table 3.1: Plate properties

post-process), the resolution of the final results and the precision of the finite difference calculations.

In the case of the FE simulation, in order to obtain a uniform grid of nodes, the elements can be any size that is a divisor of the plate dimension; for instance, the 400 mm length of the plate can be divided in elements of 200 mm, 100 mm, 80 mm, 50 mm, 40 mm, 20 mm, 10 mm, 5 mm, 2 mm, 1 mm, 0.5 mm, etc. The main limitation in this aspect is that the student version of Ansys® being used only allows simulations of up to 128K nodes/elements; to satisfy this condition, with square elements, the plate in question can have a minimum element size of 0.79 mm.

To test this aspect, and to make use of the common divisors of the plate's length and width, the element dimensions to be tested are: 40, 20, 10, 5, 2 and 1 mm. Table 3.2 shows the number of nodes for each element size and both plates, which are predicted to be proportional to the computation time. Only the Center damage case is tested, with the use of the Reduction of Laminated Stiffness damage model with a damage parameter $d = 0.1$, and the results are post-processed using all three damage detection methods. These choices are made with the objective of keeping the number of variables low, while safeguarding the most important aspects: simulation quality and testing of the damage detection methods' response to these mesh sizings. The damage parameter value is chosen as such because of similar examples in literature [8].

Element size (mm)	Number of nodes
40	66
20	231
10	861
5	3321
2	20301
1	80601

Table 3.2: Element sizes and number of nodes for the simulations

Regarding the optimal element size for the quality of the results, an analysis of this plate was already done by Moreno-García et al. [8]. The element size should be a compromise between two possible sources of error: a greater accuracy of the finite differences calculations is achieved for smaller elements, limited by the precision of the results. The calculations for the optimal element size are made considering several factors, namely: the accuracy of the results, the order of the derivative being used, the shape of the mode being studied, and the direction of the spatial derivative. This paper then presents graphics showing the results of these calculations for the first two modes, in function of the results precision. These show that different element sizes should be used for the different modes and orders of derivation; however, to simplify the analysis made in this thesis, only one size is chosen for the entire study, and the corresponding trade-offs are taken into consideration. This choice is made in Section 4.1.

3.3.3 Damage Mechanics

The different damage mechanics are tested in FE simulations and the damage detection is made using the TD, RD and CD method. Table 3.3 lists the different parameters that are used in the simulations. All of these are applied to only the center damage case. Regarding the Microphenomenology damage model, as the different damage modes are represented by different sets of micromechanics damage parameters ($\tilde{d}$ and $\tilde{d}'$ vs. $\bar{d}$ and $\bar{d}'$), the ones being used in each mode are shown in bold, and correspond to the mesoscale parameters d and d' from Equation (2.10).

Table 3.3: Damage models and parameters study

Damage Model	Damage Mode	$2/\rho$	$\tilde{d}$	$\tilde{d}'$	$\bar{d}$	$\bar{d}'$	Damage Case
Microphenomenology	1		**0.1**	**0.05**			1
			0.3	**0.15**			2
			0.5	**0.25**			3
			0.7	**0.35**			4
	2	0.2	0	0	**0.17**	**0.29**	5
		0.4			**0.3**	**0.51**	6
		0.6			**0.41**	**0.67**	7
		1			**0.58**	**0.79**	8
	1+2	0.4	0.3	0.15	**0.31**	**0.52**	9
			0.7	0.35	**0.38**	**0.62**	10
		1	0.3	0.15	**0.61**	**0.81**	11
			0.7	0.35	**0.68**	**0.85**	12
	$d^{(e)}$						
Reduction of Laminated Stiffness			0.05				13
			0.1				14
			0.3				15
			0.5				16
			0.7				17
			0.9				18

Damage Mode 1 of the Microphenomenology model is designed to simulate a severe case of delam-

ination, and as such the higher damage parameter study on this mode is the best approximation of a simulation of Teflon® tape inclusion as discussed in Section 2.4.3.

The results of each test are used as a basis to determine whether and how additional simulations of different damage parameters should be tested.

3.3.4 Damage indicators

The three damage indices, see Sections 2.6.1 to 2.6.3, are used in their full range of derivative orders, with the damage parameters from the previous test that are seen to be more relevant.

3.3.5 Noise Inclusion

The noise levels tested range from 1 up to a value where the data processing turns out to not produce any more results with quality.

The statistical analysis of the series of post-production runs is organized in graphs, showing the evolution of the damage detection quality indicators with the different noise levels, as well as different damage parameters and damage detection methods.

Chapter 4

Results

4.1 Element size analysis

The simulations described in this section are performed with all damage indices, with the element sizes from Table 3.2, and with only one damage scenario. Figure 4.1 shows that the computation time has approximately a quadratic relation with the element size, for the three damage indices. As with the DFD method figures are generated for all ten modes - contrary to the other two damage indices -, the computation time is much higher and should be the main bottleneck when considering this criterion.[1]

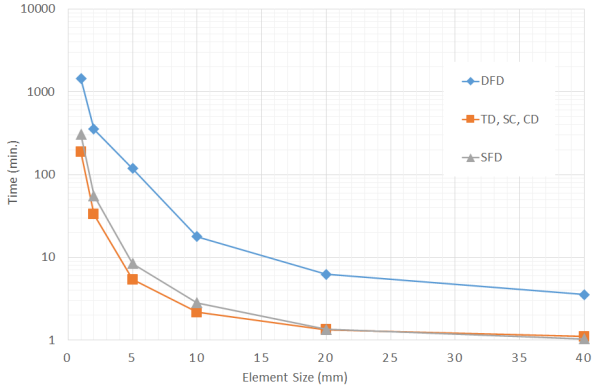

Element	Time to compute		
Size (mm)	DFD	TD, SC, CD	SFD
40	3.6 min.	1.1 min.	1 min.
20	6.2 min.	1.3 min.	1.4 min.
10	17.8 min.	2.2 min.	2.8 min.
5	1.9 hr.	5.4 min.	8.4 min.
2	5.9 hr.	33 min.	55.4 min.
1	24.1 hr.*	3.1 hr.	5.1 hr.

Figure 4.1: Computation time according to element size

Figure 4.2 shows the curvature in the x direction of the first mode for the clamped plate, with all element sizes considered; the results are presented in this way in order to allow for both the mesh's overall appearance and the quality of the derivation operation to be evaluated. The 1 mm and 2 mm figures show that this mesh is so fine that, at this size figure, it can barely be made out. Generally, the predicted assumptions are verified, as the coarser meshes show less detail, as well as less smooth (i.e. more stepped) curves in the shapes resulting of the derivation operations.

[1] The simulation for the 1 mm element size with the DFD method was not performed, and as such this time is estimated based on the other simulations. Given the number of simulations projected for the analysis intended in this thesis, this computation time is not in the desirable range, and the element size is not of interest, thus this simulation is not necessary to be run.

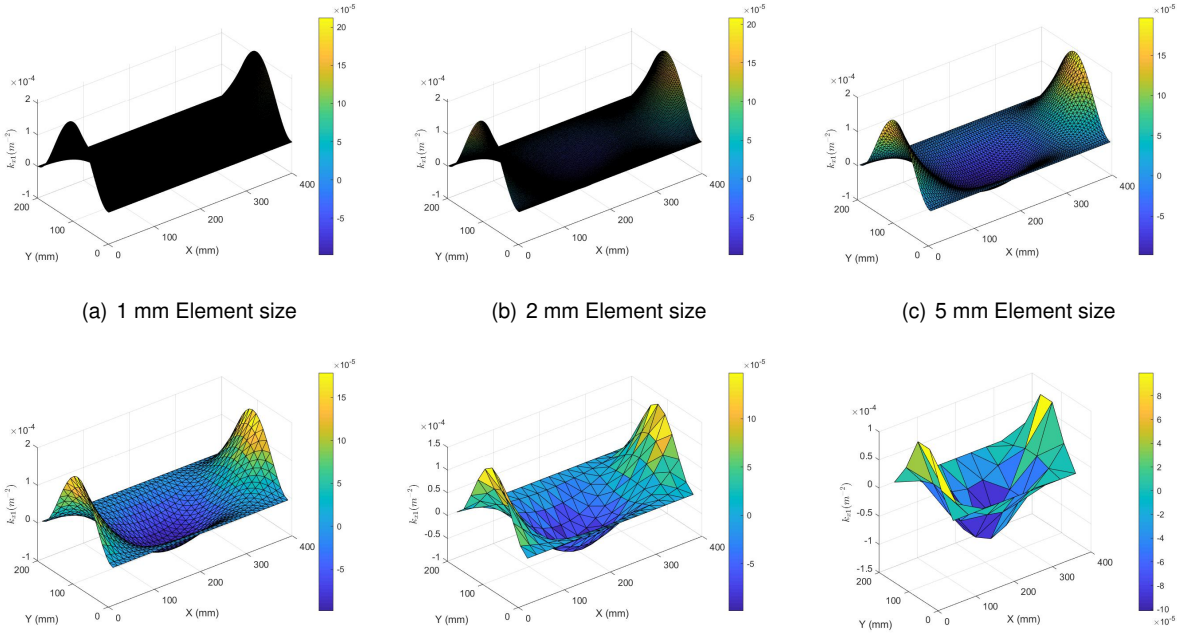

(a) 1 mm Element size (b) 2 mm Element size (c) 5 mm Element size

(d) 10 mm Element size (e) 20 mm Element size (f) 40 mm Element size

Figure 4.2: First mode curvatures for different element sizes.

The results of these simulations are obtained with double precision (i.e. with 15 significant digits). For the first two modes, the analysis of this plate done by Moreno-García et al. [8] shows that, for the characteristics of this data set, the optimal element size is on the order of 1 mm. For higher derivation orders the optimal element size is larger - for the fourth derivative it is about 5-10 times larger than for the first derivative. To account for the loss of effective precision when the noise is added to the results, as well as a computation time within the intended time frame, the chosen element size to be used for the remaining simulations is 5 mm.

4.2 Damage Mechanics Analysis

For this part of the analysis, all of the damage cases in Table 3.3 are simulated and the damage detection is made using the TD, SD and CD method, for a relatively simple comparison between damage cases. The damage scenario is that of a center square damaged area of 40 mm * 40 mm. Figure 4.3 shows the damaged area location, as well as the results of the damage detection for Damage Case 1 - the least severe of the ones tested.

The figures showing the damage detection using this technique are very similar across all damage cases. The TD graphic shows some improvements for more severe damage cases, but is generally very unreliable, as shown in Figure 4.4, where different levels of damage severity are shown.

One of the main differences between the different Damage Cases is the maximum value that the damage index reaches. This value is used in place of the Quality Index μ, because μ has a very similar value across all damage cases - with a maximum variation of about 4% - while the value for the maximum SD or CD varies by several orders of magnitude. The index μ is more useful when quantifying damage

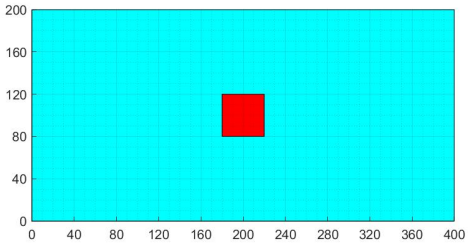

(a) Damage Scenario being tested

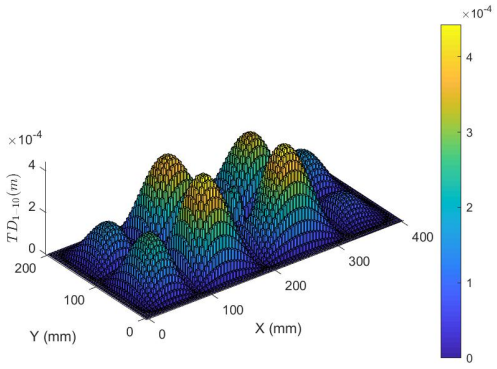

(b) Damage detection using Translation Differences

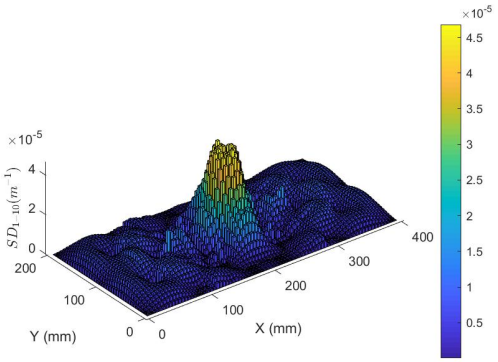

(c) Damage detection using Slope Differences

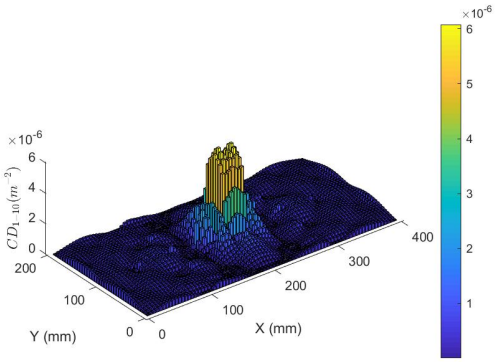

(d) Damage detection using Curvature Differences

Figure 4.3: Damage Detection for Damage Case 1

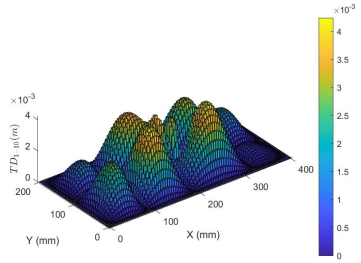

(a) Damage Case 12

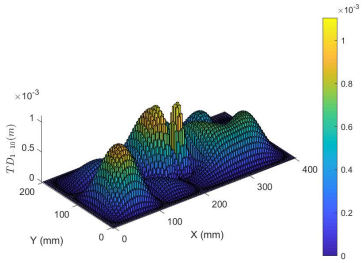

(b) Damage Case 13

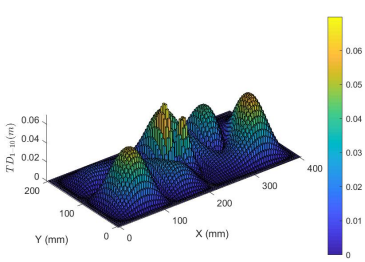

(c) Damage Case 18

Figure 4.4: Damage Detection using Translation Differences

detection instances with more significant differences in quality; in this case, as the general appearance of the graphs is very similar, - which is an indicative of similar quality - analysing the values for the maximum SD and CD gives a better context to the magnitude of the differences between the severity of the damage cases. Figure 4.5 shows this value for all damage cases. For each damage mode, as well as in the RLS damage model, it is clear that the severity of the damage increases with the damage parameters, as expected.

This graph also shows that, while using the Microphenomenology model, the increase in the maximum SD and CD is not as pronounced as when using the RLS model; having in mind that the main

difference between the two damage models is the manipulation of E_1, - which happens with the RLS model but not with the Microphenomenology one - this factor seems to have a specially notable impact on the severity of the damage. Comparing Damage Cases 8 and 17, which have comparable damage parameters (around 0.7), the former has about 10 times smaller values of maximum SD and DC, which shows the magnitude of the impact the manipulation of E_1 has on the structure.

To analyze the operations made in the Microphenomenology model, damage cases 2 through 4 are compared to cases 5 through 7, as the variations in the damage parameters are similar, only inverting d and d' (on the former, $d \in [0.3, 0.7]$, $d' \in [0.15, 0.35]$ and on the latter $d \in [0.17, 0.41]$, $d' \in [0.29, 0.67]$). The values in Figure 4.5 show that the second set of damage cases has a higher severity by about 20% to 30%; these results suggest that the higher values of d' have a larger impact on the severity of the damage than those of d, i.e. the manipulation of E_2 has more impact than that of G_{12} in the actual severity of the damage. According to the analysis made by the original authors developing this damage model [20], these results suggest that a loss of tenacity in the matrix, paired with microcracking, has a larger impact than fiber-matrix debonding leading to a loss of shear stiffness; this deduction is however made using a small sample and is based on having similar values assigned to the damage parameters, so a more comprehensive study of this phenomenon is needed to further elaborate on this hypothesis.

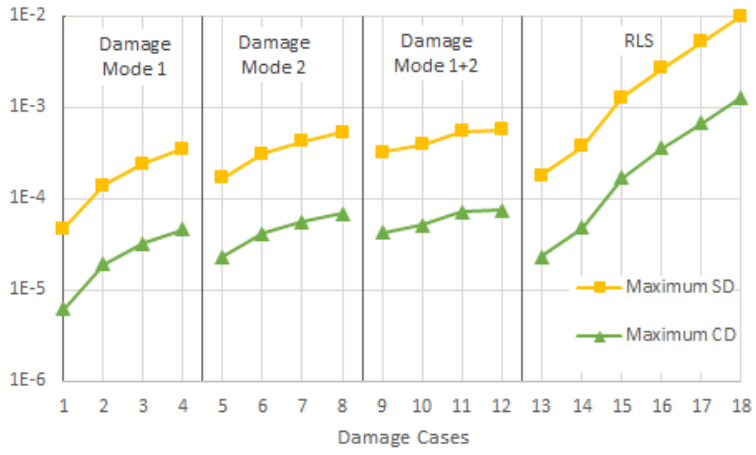

Damage Case	Maximum SD	Maximum CD
1	$4.7 * 10^{-5}$	$6.1 * 10^{-6}$
2	$1.4 * 10^{-4}$	$1.9 * 10^{-5}$
3	$2.4 * 10^{-4}$	$3.2 * 10^{-5}$
4	$3.5 * 10^{-4}$	$4.6 * 10^{-5}$
5	$1.7 * 10^{-4}$	$2.3 * 10^{-5}$
6	$3.1 * 10^{-4}$	$4.1 * 10^{-5}$
7	$4.2 * 10^{-4}$	$5.5 * 10^{-5}$
8	$5.3 * 10^{-4}$	$6.9 * 10^{-5}$
9	$3.2 * 10^{-4}$	$4.2 * 10^{-5}$
10	$3.9 * 10^{-4}$	$5.1 * 10^{-5}$
11	$5.5 * 10^{-4}$	$7.2 * 10^{-5}$
12	$5.7 * 10^{-4}$	$7.4 * 10^{-5}$
13	$1.8 * 10^{-4}$	$2.3 * 10^{-5}$
14	$3.7 * 10^{-4}$	$4.8 * 10^{-5}$
15	$1.3 * 10^{-3}$	$1.7 * 10^{-4}$
16	$2.7 * 10^{-3}$	$3.6 * 10^{-4}$
17	$5.2 * 10^{-3}$	$6.7 * 10^{-4}$
18	$1.0 * 10^{-2}$	$1.3 * 10^{-3}$

Figure 4.5: Damage cases severity study

Having in mind the considerations of the previous paragraphs, damage cases 8 (Microphenomenology, $d' = 0.79$ and $d = 0.58$) and 17 (RLS, $d^{(e)} = 0.7$) are used to test the different damage detection

methods, as they offer different levels of damage severity, as well as different damage mechanics.

4.3 Damage indices

The three damage indices employ different choices regarding the approach to the vectorial components of the spatial derivatives, and single mode *vs.* multiple mode analysis. Using the two damage cases chosen on the end of Section 4.2, and both boundary conditions - clamped edges and free plate - the merits and shortcomings of each damage index are discussed. Figures 4.6 and 4.7 show the mode shapes and frequencies for the first ten modes for the plates with clamped and free edges as boundary conditions, respectively. These modes are the baseline for the damage indices, to which all damage cases are compared, either by comparing the frequencies or by performing derivation operations and calculating the difference with the ones present here.

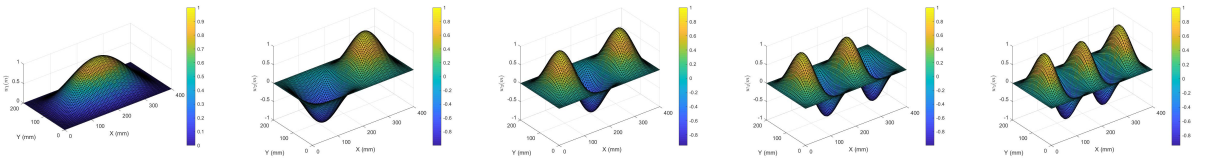

(a) w_1, $f_1 = 159.9$ Hz (b) w_2, $f_2 = 178.9$ Hz (c) w_3, $f_3 = 224.4$ Hz (d) w_4, $f_4 = 301.6$ Hz (e) w_5, $f_5 = 409.5$ Hz

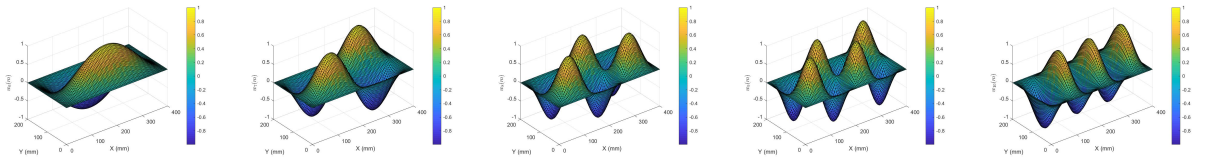

(f) w_6, $f_6 = 433.6$ Hz (g) w_7, $f_7 = 446.0$ Hz (h) w_8, $f_8 = 473.8$ Hz (i) w_9, $f_9 = 524.2$ Hz (j) w_{10}, $f_{10} = 546.2$ Hz

Figure 4.6: Displacement fields without damage for the first ten modes of the clamped plate.

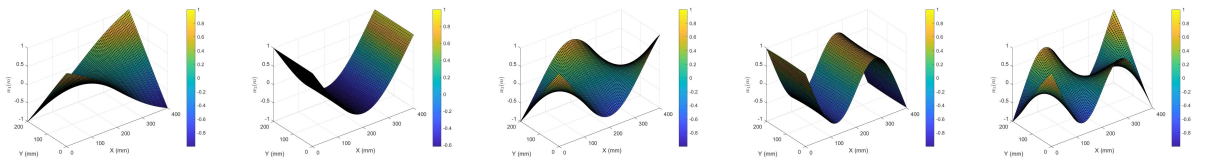

(a) w_1, $f_1 = 20.9$ Hz (b) w_2, $f_2 = 26.9$ Hz (c) w_3, $f_3 = 50.6$ Hz (d) w_4, $f_4 = 74.3$ Hz (e) w_5, $f_5 = 98.1$ Hz

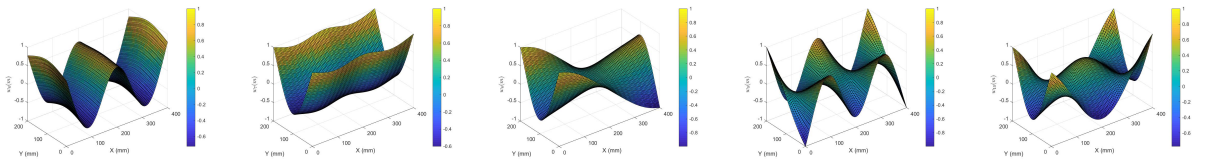

(f) w_6, $f_6 = 145.6$ Hz (g) w_7, $f_7 = 155.7$ Hz (h) w_8, $f_8 = 161.0$ Hz (i) w_9, $f_9 = 168.3$ Hz (j) w_{10}, $f_{10} = 179.6$ Hz

Figure 4.7: Displacement fields without damage for the first ten modes of the free plate.

4.3.1 Difference in Field Derivatives

As the damage detection is performed mode-by-mode, the figures shown are of the better examples of each aspect being analyzed, either vibration modes, derivation degrees or damage cases. Using this damage index, a further analysis of different mode shapes' influence on damage detection in made on Section 2.2. As shown in Figure 4.1, this method is the one which takes the longest to compute, as the damage index calculations and figure generation are made for all ten modes instead of only one for all modes, as on the other two damage indices. For ten modes, four different orders of derivatives for each mode, three damage scenarios, two sets of boundary conditions, and two damage cases, the number of figures to be shown would be too large to show all of them, so only the most representative cases are shown. Analyzing Figures 4.6 and 4.7, to find variety in the mode shapes, modes 1 and 4 of the clamped plate will be further studied in this subsection, as well as modes 2 and 8 of the free plate. These specific mode shapes show different values of the displacement in the center of the plate, as well as different values for the first two derivatives in the x direction - which are inferred through visual inspection.

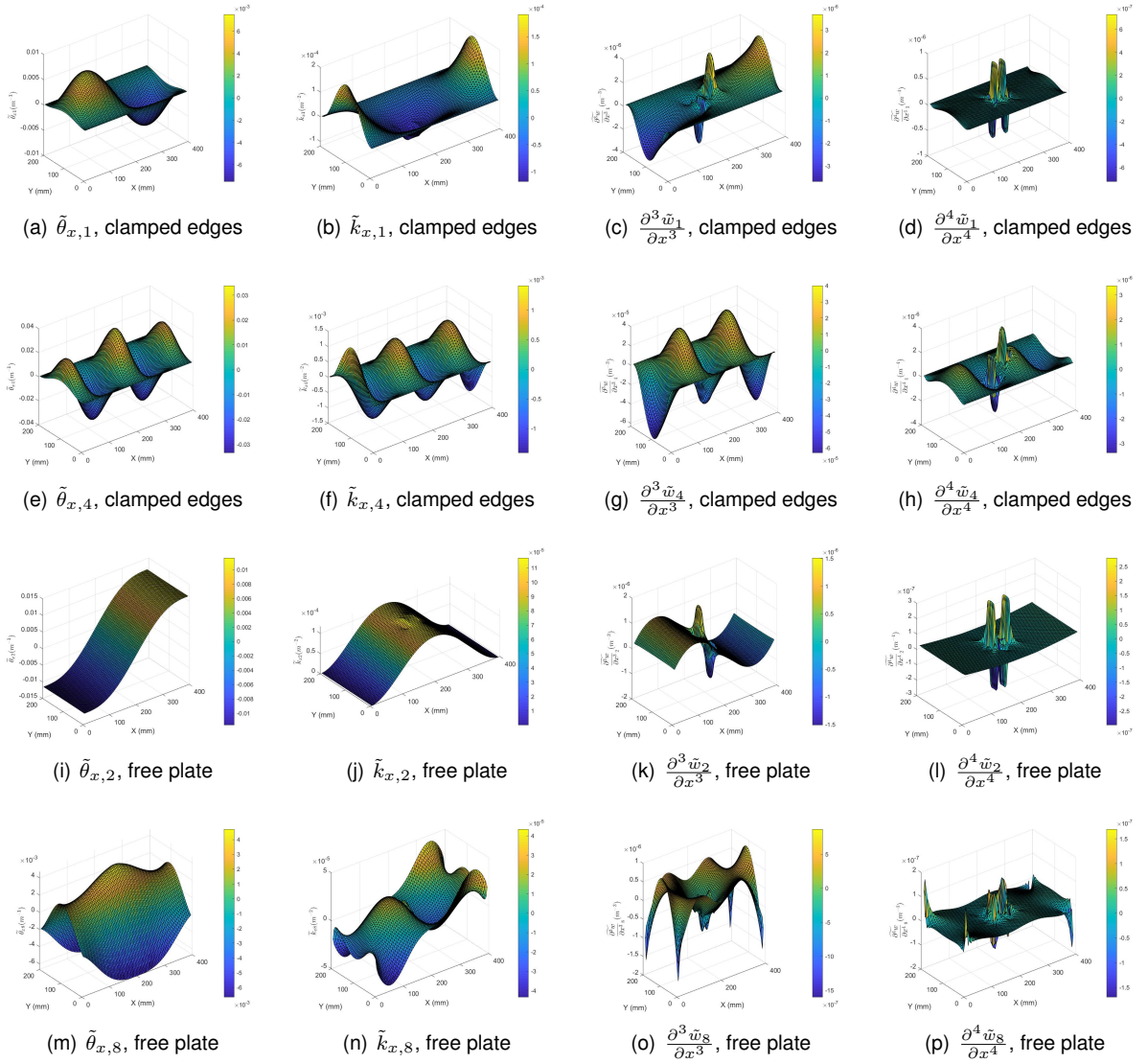

(a) $\tilde{\theta}_{x,1}$, clamped edges (b) $\tilde{k}_{x,1}$, clamped edges (c) $\frac{\partial^3 \tilde{w}_1}{\partial x^3}$, clamped edges (d) $\frac{\partial^4 \tilde{w}_1}{\partial x^4}$, clamped edges

(e) $\tilde{\theta}_{x,4}$, clamped edges (f) $\tilde{k}_{x,4}$, clamped edges (g) $\frac{\partial^3 \tilde{w}_4}{\partial x^3}$, clamped edges (h) $\frac{\partial^4 \tilde{w}_4}{\partial x^4}$, clamped edges

(i) $\tilde{\theta}_{x,2}$, free plate (j) $\tilde{k}_{x,2}$, free plate (k) $\frac{\partial^3 \tilde{w}_2}{\partial x^3}$, free plate (l) $\frac{\partial^4 \tilde{w}_2}{\partial x^4}$, free plate

(m) $\tilde{\theta}_{x,8}$, free plate (n) $\tilde{k}_{x,8}$, free plate (o) $\frac{\partial^3 \tilde{w}_8}{\partial x^3}$, free plate (p) $\frac{\partial^4 \tilde{w}_8}{\partial x^4}$, free plate

Figure 4.8: First four derivatives of the displacement for the selected modes of the damaged plate with DC8 and center damage scenario, using the x component of the derivation vectors.

Figure 4.8 shows the first four derivatives of the displacement field for the selected modes of the damaged plate, with the lighter of the two selected damage cases being employed. These graphics show how sensitive the higher order derivatives are to damage, with the damaged area exhibiting very noticeable disturbances to the otherwise smooth contours, more so for some modes than for others, with the first mode of the plate with clamped edges exhibiting the highest sensitivity and the eighth mode of the free plate the lowest.

Figure 4.9 shows the damage detection of DC8 and center damage scenario using the DFD index in the selected modes. For each mode, the improvement in quality of damage detection is notorious when successively higher order derivatives are employed. Comparing different modes, some show better damage detection than others, mainly when using the displacement field or lower order derivatives, with the extremes being found in the same modes as in the analysis made of Figure 4.8. Figures 4.9(u) and 4.9(v) show that, for each mode, higher order derivatives almost always yield higher quality damage detection - according to the use of μ_q -, although the variation between modes is considerable and the improvement in quality achieved by employing higher order derivatives is also highly variable. These results suggest that the most complete sets possible of derivative orders and mode shapes should be employed for effective damage detection and localization, so that the different indices' responses can be compared by visual inspection and this type of inconsistency is qualitatively evaluated.

To evaluate the responsiveness of the DFD index to different damage locations, simulations for the Damage Scenarios listed in Table 3.1 are run, for both the corner and the center + corner scenarios, using the clamped boundary conditions. Figure 4.10 shows the damage detection for the former, with modes 3 and 8 being of the plate with clamped edges used to illustrate the different responses that some modes show to this damage scenario; fig. 4.10(k) shows that, for the first ten modes, the response of the different derivation orders is about as uniform across the modes as that of of the center damage scenario, however the results of $DFD_q^{(0)}$ and $DFD_q^{(1)}$ of the remaining modes are generally as low quality as the ones shown here. The high values of the damage indicator across the plate for these lower order derivatives show that this damage scenario is more difficult do detect than the one in the center, and the cause may be the mode shapes themselves, as they present lower values of displacement on the corners than on the center of the plate.

Figure 4.11 shows the damage detection of the center + corner scenario using the DFD method and modes 1, 2 and 8 of the plate with clamped edges, as well as a schematic of the scenario. The detectability of the corner damage is clearly overshadowed by that of the center, on some modes and derivation degrees more than others; as both damaged areas are the same size and have the same damage case (DC8), the discrepancy in the damage detectability of the two areas can only be assumed to be due to the mode shapes of the first ten modes, as mode 8 is chosen specifically as the one where the corner damage is the most detectable. The modes shown in Figure 4.11 are used to illustrate different degrees of this phenomenon, and the order by which they are shown is by ascending quality of the detection of the corner damage; however even in mode 8 the corner damage is considerably less detectable than the center one. An imbalance on damage severity towards a more meaningful damage on the corner than on the center shifts the relative detectability of the two, but the characteristics of the

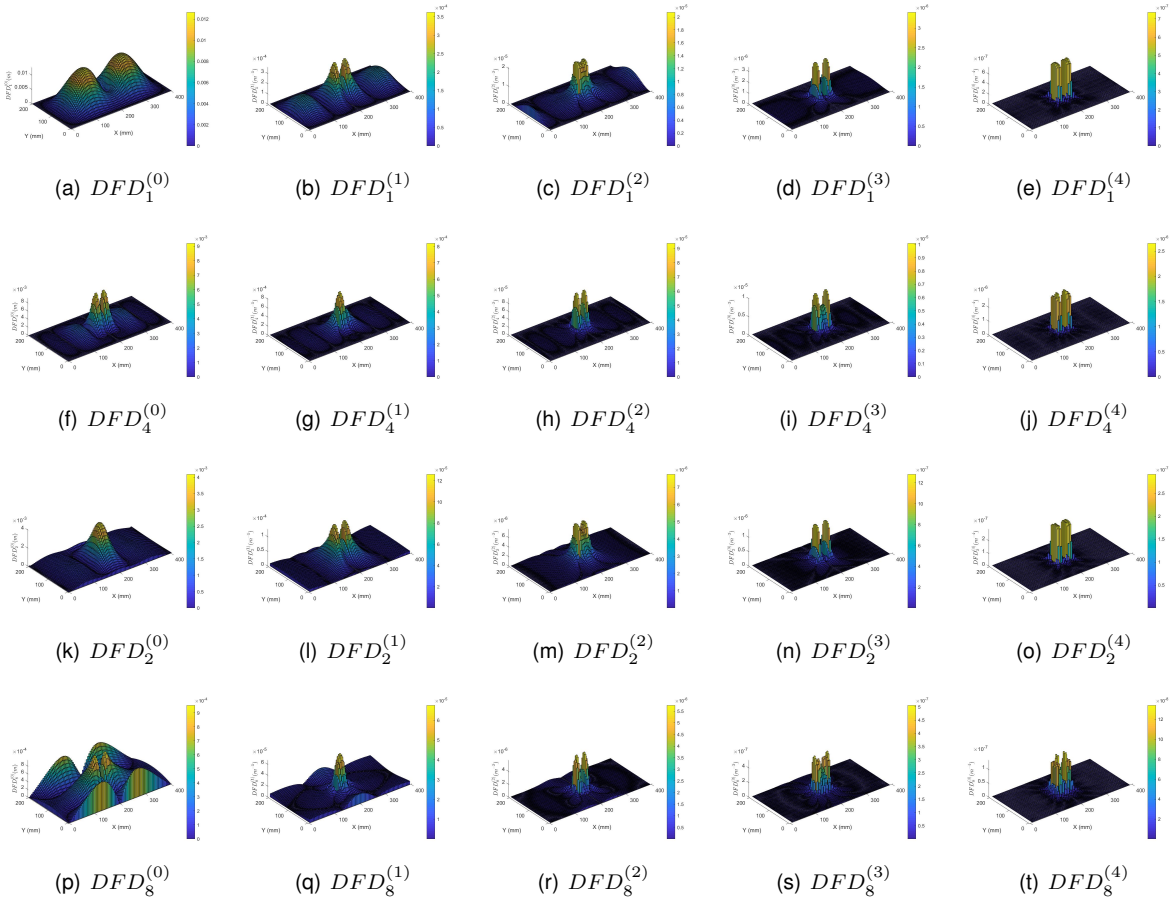

(a) $DFD_1^{(0)}$ (b) $DFD_1^{(1)}$ (c) $DFD_1^{(2)}$ (d) $DFD_1^{(3)}$ (e) $DFD_1^{(4)}$

(f) $DFD_4^{(0)}$ (g) $DFD_4^{(1)}$ (h) $DFD_4^{(2)}$ (i) $DFD_4^{(3)}$ (j) $DFD_4^{(4)}$

(k) $DFD_2^{(0)}$ (l) $DFD_2^{(1)}$ (m) $DFD_2^{(2)}$ (n) $DFD_2^{(3)}$ (o) $DFD_2^{(4)}$

(p) $DFD_8^{(0)}$ (q) $DFD_8^{(1)}$ (r) $DFD_8^{(2)}$ (s) $DFD_8^{(3)}$ (t) $DFD_8^{(4)}$

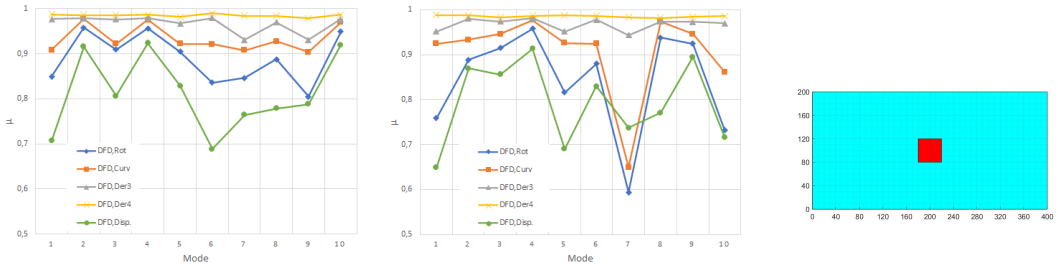

(u) Quality indicator of the first ten modes for the clamped plate

(v) Quality indicator of the first ten modes for the free plate

(w) Damage Scenario

Figure 4.9: Damage detection with the DFD index for DC8 and center damage scenario.

mode shapes of the clamped plate - derived from the fact that the plate is clamped - always favour the detection of the center damage over the corner one. For other combinations of damaged areas, the mode shapes of the plate should be analyzed prior to the use of this technique, as the lack of peaks or valleys in certain areas of the displacement fields of the used modes could be used to predict the blind spots found here.

Figure 4.12 shows the same analysis, with the free plate being used, and thus generating completely different mode shapes. The three modes shown, 1, 2 and 4, show the three possible outcomes of this damage detection, respectively: only the corner damage being effectively detected, only the center one, and a balanced detection, with some differences being found when different derivative degrees are being used. This goes to show the influence of the mode shapes in the detectability of the damage:

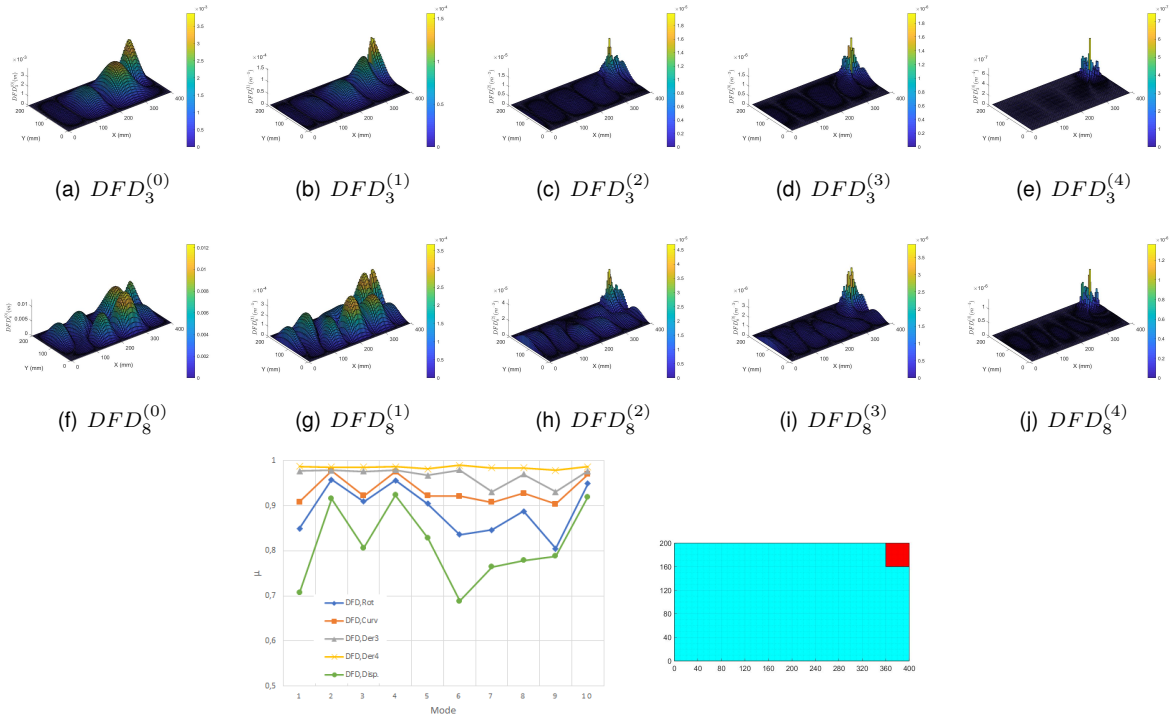

(a) $DFD_3^{(0)}$ (b) $DFD_3^{(1)}$ (c) $DFD_3^{(2)}$ (d) $DFD_3^{(3)}$ (e) $DFD_3^{(4)}$

(f) $DFD_8^{(0)}$ (g) $DFD_8^{(1)}$ (h) $DFD_8^{(2)}$ (i) $DFD_8^{(3)}$ (j) $DFD_8^{(4)}$

(k) Quality indicator of the first ten modes

(l) Damage Scenario

Figure 4.10: Damage detection with the DFD index for DC8 and corner damage scenario, for the plate with clamped edges.

the fact that the edges are free allows the existence of peaks and valleys on all areas of the plate, which eliminates possible blind spots in damage detection, which show a potential to be located in the clamped areas of the plate. This behaviour should be had in mind when applying this technique to real world structures, which could be considered for *in loco* use of this technique: the zones of a structure in which higher stress are generally found are those which are clamped (for example, the root of an airplane wing) and, should damage arise from these higher stresses, it would be harder to detect through mode shape analysis than if it was on an area of the structure more free to vibrate.

The data sets of the quality indicator for the center and corner damage scenarios were compared to the average value of each of the derivatives on the damaged area for each mode, for both the clamped and the free plate, and no strong correlation is found between them; for this reason, there is no basis to recommend any other technique than to visually inspect the modes for constrained areas to prevent the aforementioned blind spots from hampering the damage detection.

4.3.2 Differences between sums of Displacements, Rotations and Curvatures

This damage index differs from the previous one by three important factors: the use of the euclidean norm of the derivatives' vectors - instead of only the x component -, the employment of only two degrees of derivative - instead of four -, as well as the use of the sum of all modes for the analysis - instead of just one. As a result of the higher simplicity, the analysis is made for a more complex set of variables, namely the damage parameters. Figures 4.13 and 4.14 show the derivation operations' response to the

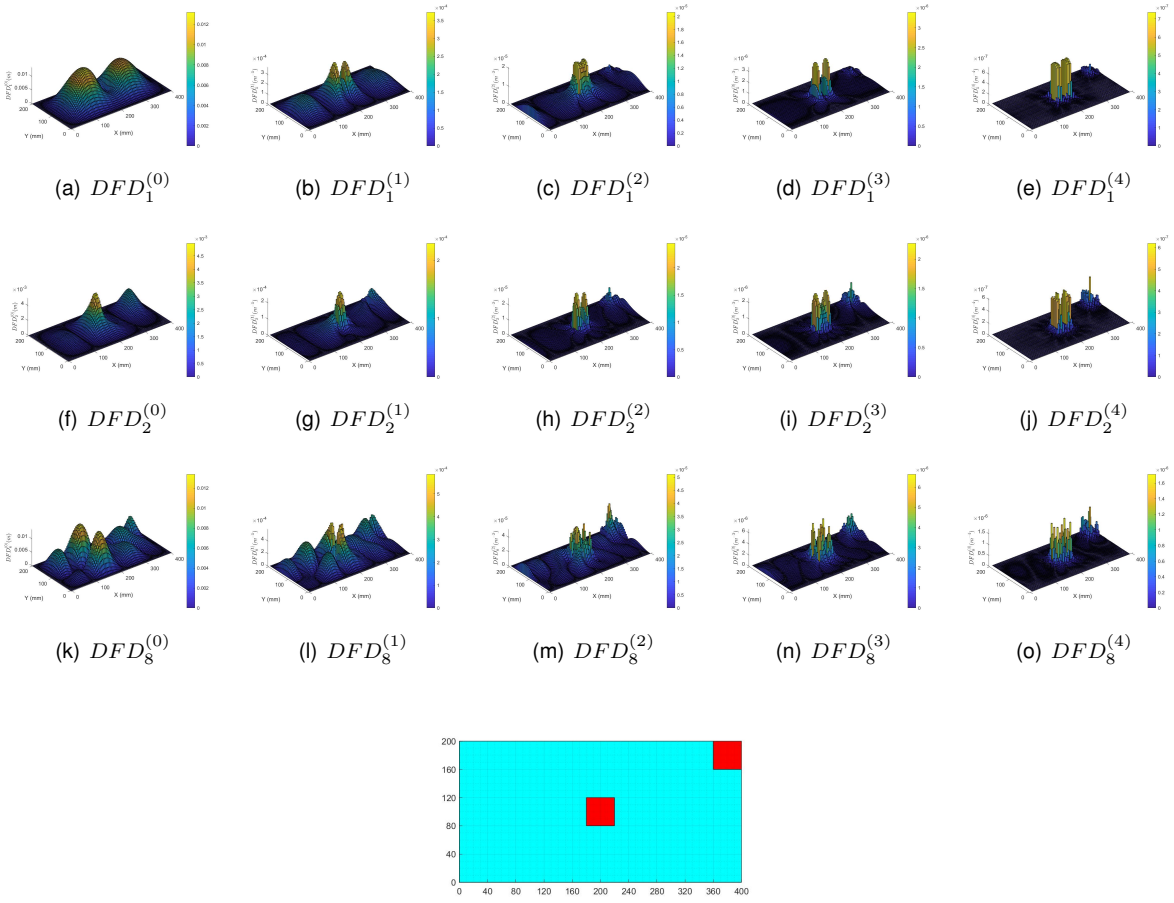

(a) $DFD_1^{(0)}$ (b) $DFD_1^{(1)}$ (c) $DFD_1^{(2)}$ (d) $DFD_1^{(3)}$ (e) $DFD_1^{(4)}$

(f) $DFD_2^{(0)}$ (g) $DFD_2^{(1)}$ (h) $DFD_2^{(2)}$ (i) $DFD_2^{(3)}$ (j) $DFD_2^{(4)}$

(k) $DFD_8^{(0)}$ (l) $DFD_8^{(1)}$ (m) $DFD_8^{(2)}$ (n) $DFD_8^{(3)}$ (o) $DFD_8^{(4)}$

(p) Damage Scenario

Figure 4.11: Damage detection with the DFD index for DC8 and center + corner damage scenario, for the plate with clamped edges.

two selected damage cases and the center damage scenario. Most of these figures do not show the severe disturbances in the mode shapes that can be seen on Figure 4.8, with the only notable exception for the curvature of the damaged plate with DC17 for both the free plate and the one with clamped edges. Due to the employment of only the first two orders of derivative - providing the rotations and curvatures -, the more pronounced disturbances of the higher order derivatives are not observed in this instance.

Figure 4.15 shows the damage detection using the TD, SD and CD index for a center damage scenario, for both clamped and free plates and for DC8 and DC17. The results of the use of the TD index show that it is largely unreliable, as there are too many peaks observed on the plate to reasonably identify the one which corresponds to the damaged area. The employment of the rotations on the SD index shows significant improvements, mostly on the clamped plate, where it shows a very clear peak on the center of the plate; in the case of the free plate, the SD index still shows some peaks throughout the plate, compromising the damage detection. The use of the CD index shows significant improvement on all cases shown here, as the damaged area on the center of the plate exhibits the only peak of this indicator; once again, the free plate produces slightly less reliable results, as there are some higher values of the index throughout the plate, however significantly lower than those at the damaged area.

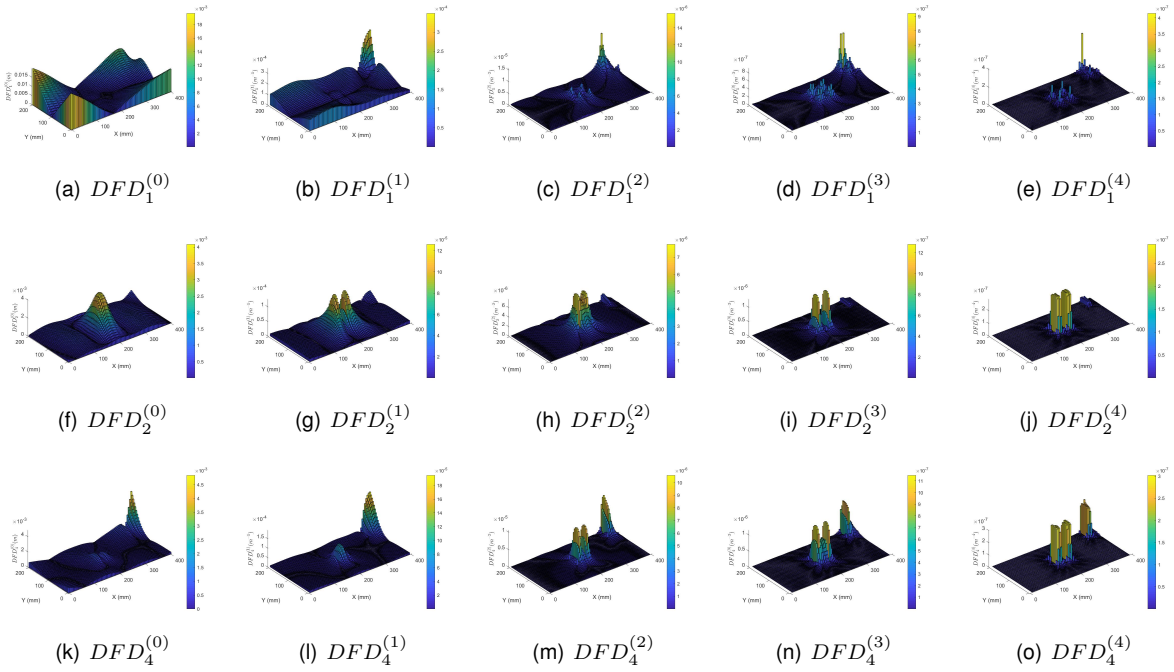

(a) $DFD_1^{(0)}$ (b) $DFD_1^{(1)}$ (c) $DFD_1^{(2)}$ (d) $DFD_1^{(3)}$ (e) $DFD_1^{(4)}$

(f) $DFD_2^{(0)}$ (g) $DFD_2^{(1)}$ (h) $DFD_2^{(2)}$ (i) $DFD_2^{(3)}$ (j) $DFD_2^{(4)}$

(k) $DFD_4^{(0)}$ (l) $DFD_4^{(1)}$ (m) $DFD_4^{(2)}$ (n) $DFD_4^{(3)}$ (o) $DFD_4^{(4)}$

Figure 4.12: Damage detection with the DFD index for DC8 and center + corner damage scenario, for the free plate.

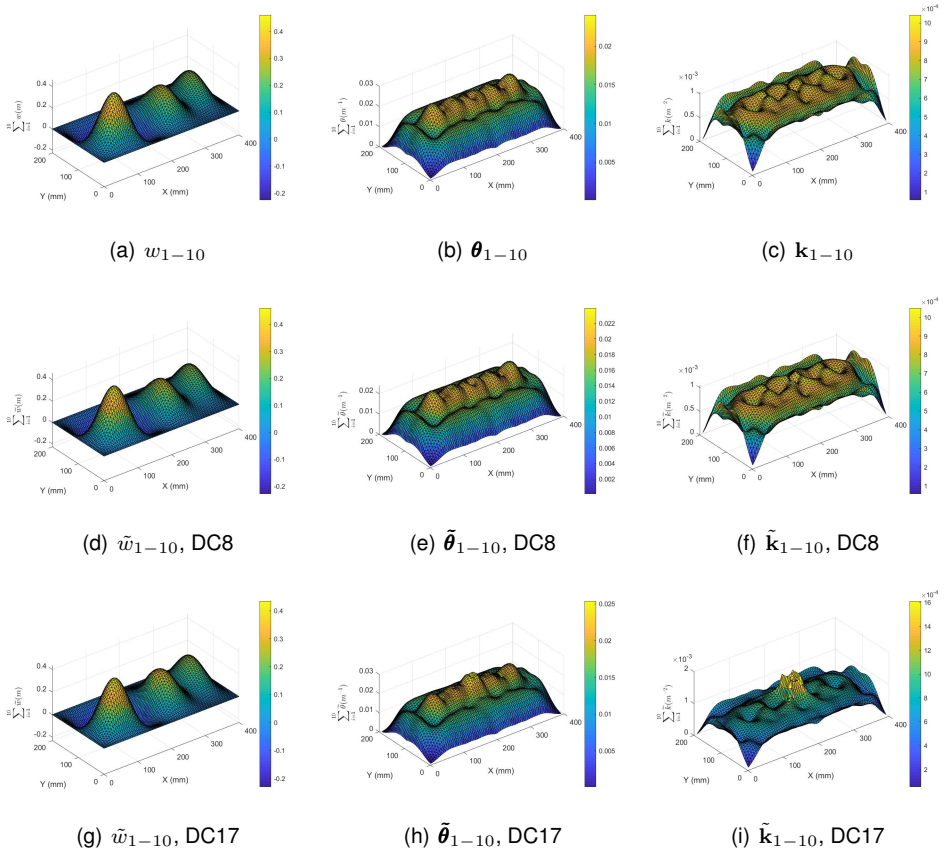

(a) w_{1-10} (b) $\boldsymbol{\theta}_{1-10}$ (c) $\mathbf{k}_{1-10}$

(d) $\tilde{w}_{1-10}$, DC8 (e) $\tilde{\boldsymbol{\theta}}_{1-10}$, DC8 (f) $\tilde{\mathbf{k}}_{1-10}$, DC8

(g) $\tilde{w}_{1-10}$, DC17 (h) $\tilde{\boldsymbol{\theta}}_{1-10}$, DC17 (i) $\tilde{\mathbf{k}}_{1-10}$, DC17

Figure 4.13: Displacement field and first two derivatives of the undamaged and damaged plate with both DC8 and DC17, and center damage scenario, using the euclidean norm of the derivation vectors, for the plate with clamped edges.

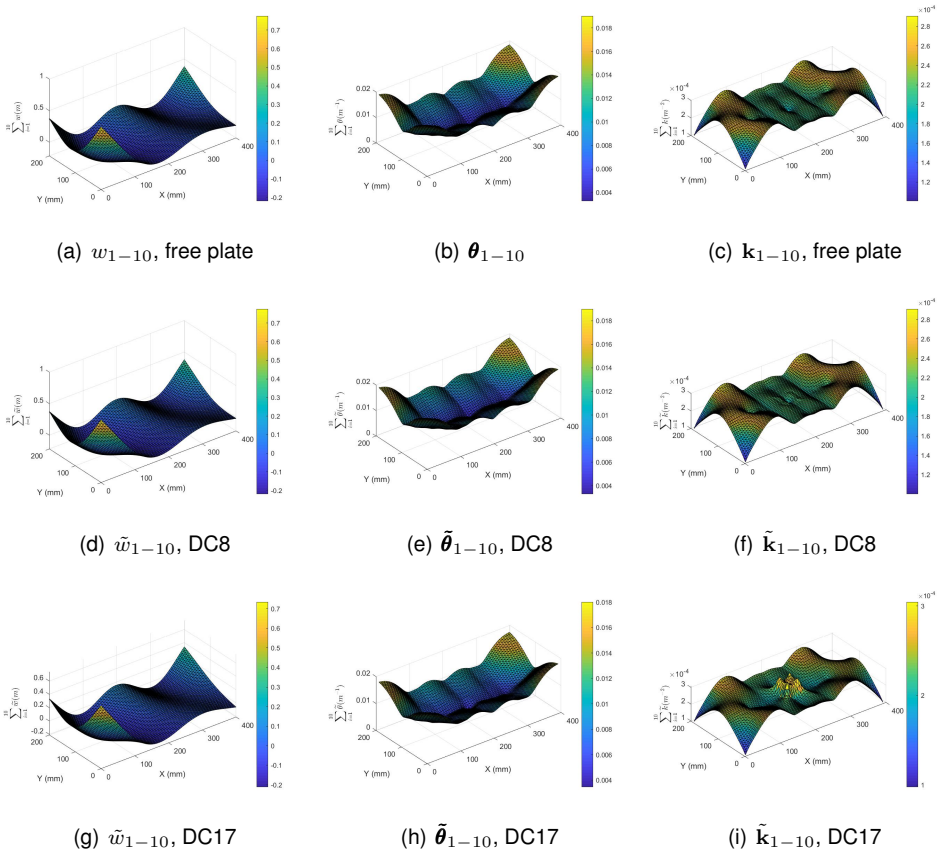

(a) w_{1-10}, free plate (b) $\boldsymbol{\theta}_{1-10}$ (c) $\mathbf{k}_{1-10}$, free plate

(d) $\tilde{w}_{1-10}$, DC8 (e) $\tilde{\boldsymbol{\theta}}_{1-10}$, DC8 (f) $\tilde{\mathbf{k}}_{1-10}$, DC8

(g) $\tilde{w}_{1-10}$, DC17 (h) $\tilde{\boldsymbol{\theta}}_{1-10}$, DC17 (i) $\tilde{\mathbf{k}}_{1-10}$, DC17

Figure 4.14: Displacement field and first two derivatives of the undamaged and damaged plate with both DC8 and DC17, and center damage scenario, using the euclidean norm of the derivation vectors, for the free plate.

Figure 4.16 shows the same process of damage detection, however for a corner damage scenario. Overall, the results are similar to the ones from the center damage scenario: the use of TD is largely unreliable; the use of SD is very reliable on the plate with clamped edges but it produces no quality results on the free one; the results of the CD index are largely satisfactory, with a slight loss of quality for the use of the free plate. An important aspect to take note is the values reached by the indicator at the damage location, both on Figure 4.15 and Figure 4.16: on all cases, DC17 produces about 10x higher peak values than DC8 (for each scenario and boundary conditions), to similar values across the rest of the plate, thus creating a higher quality of damage detection.

Figure 4.17 shows the damage detection for the center + corner damage scenario, with equal damaged areas of 40 mm*40 mm. As before, the use of the TD index is mostly useless for this application. The use of the SD index is only reliable when the edges of the plate are clamped and, as in the use of the DFD index, the detection of the center damaged area is much more effective than that of the corner one for these boundary conditions. Once again, the use of the CD index produces the best results, with diverging results according to the boundary condition used: when the edges are clamped, the center damaged area is has a much higher peak than that of the corner (just as with SD); when the plate is free, the opposite occurs. These results are similar to those obtained when using DFD in Section 4.3.1, where it was concluded that the clamped areas have a potential of concealing damaged areas. Con-

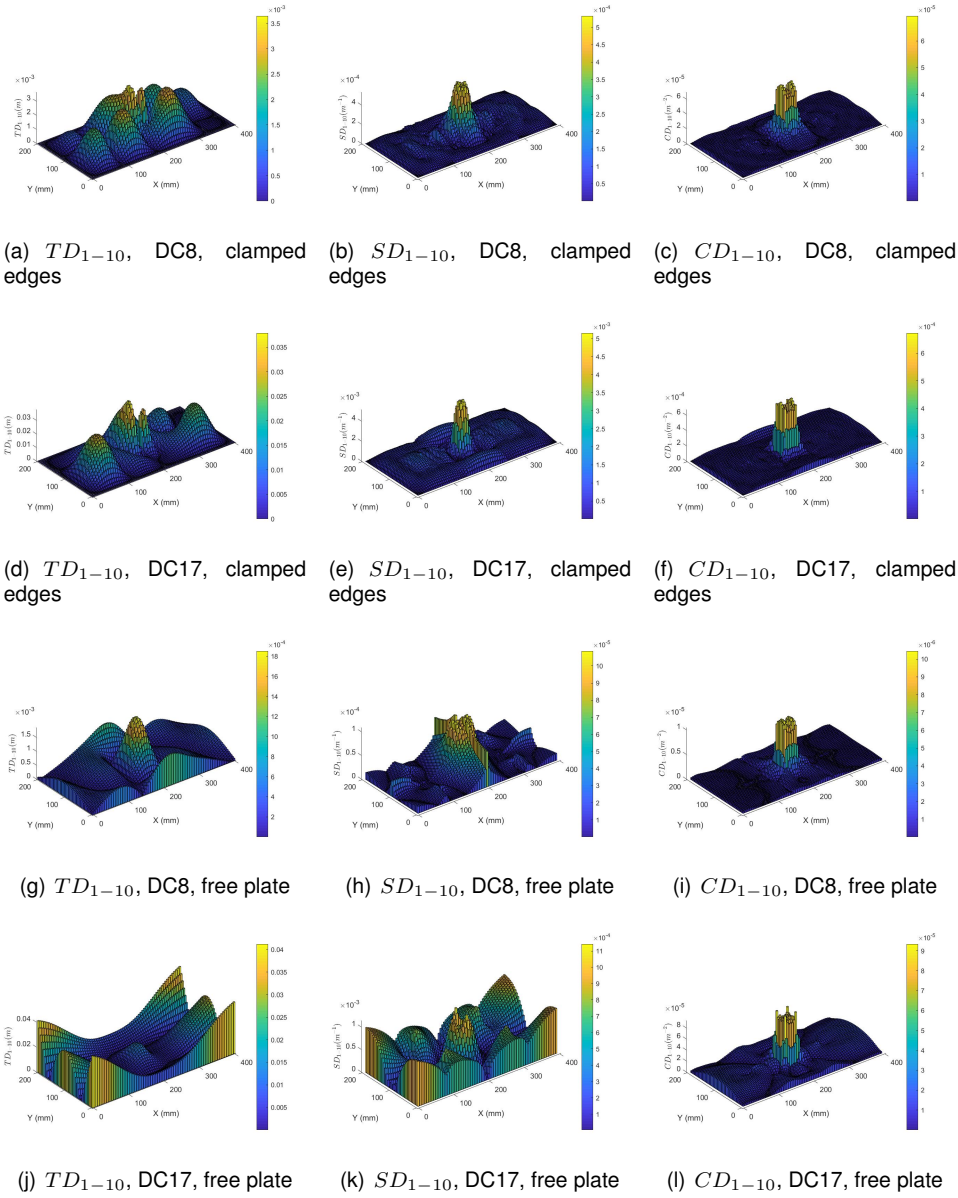

(a) TD_{1-10}, DC8, clamped edges (b) SD_{1-10}, DC8, clamped edges (c) CD_{1-10}, DC8, clamped edges

(d) TD_{1-10}, DC17, clamped edges (e) SD_{1-10}, DC17, clamped edges (f) CD_{1-10}, DC17, clamped edges

(g) TD_{1-10}, DC8, free plate (h) SD_{1-10}, DC8, free plate (i) CD_{1-10}, DC8, free plate

(j) TD_{1-10}, DC17, free plate (k) SD_{1-10}, DC17, free plate (l) CD_{1-10}, DC17, free plate

Figure 4.15: Damage detection with the TD, SD and CD index for DC8 and DC17, and center damage scenario, for both the plate with clamped edges and the free plate.

cerning the higher sensibility of the free plate to the corner damage, the only explanation found is that, out of the first ten modes with these boundary conditions, the ones where the corner damage is better identified have a higher expression than the opposite.

No further simulations are deemed to be necessary to further the study of this damage index at this stage. The multiple damage detection has been established as being dependant on boundary conditions, and as such there is no need to test different levels of damage severity on the two damaged areas. An evaluation on the choice of whether to employ all vectorial components of the derivatives in an euclidean norm is performed on Section 4.3.3.

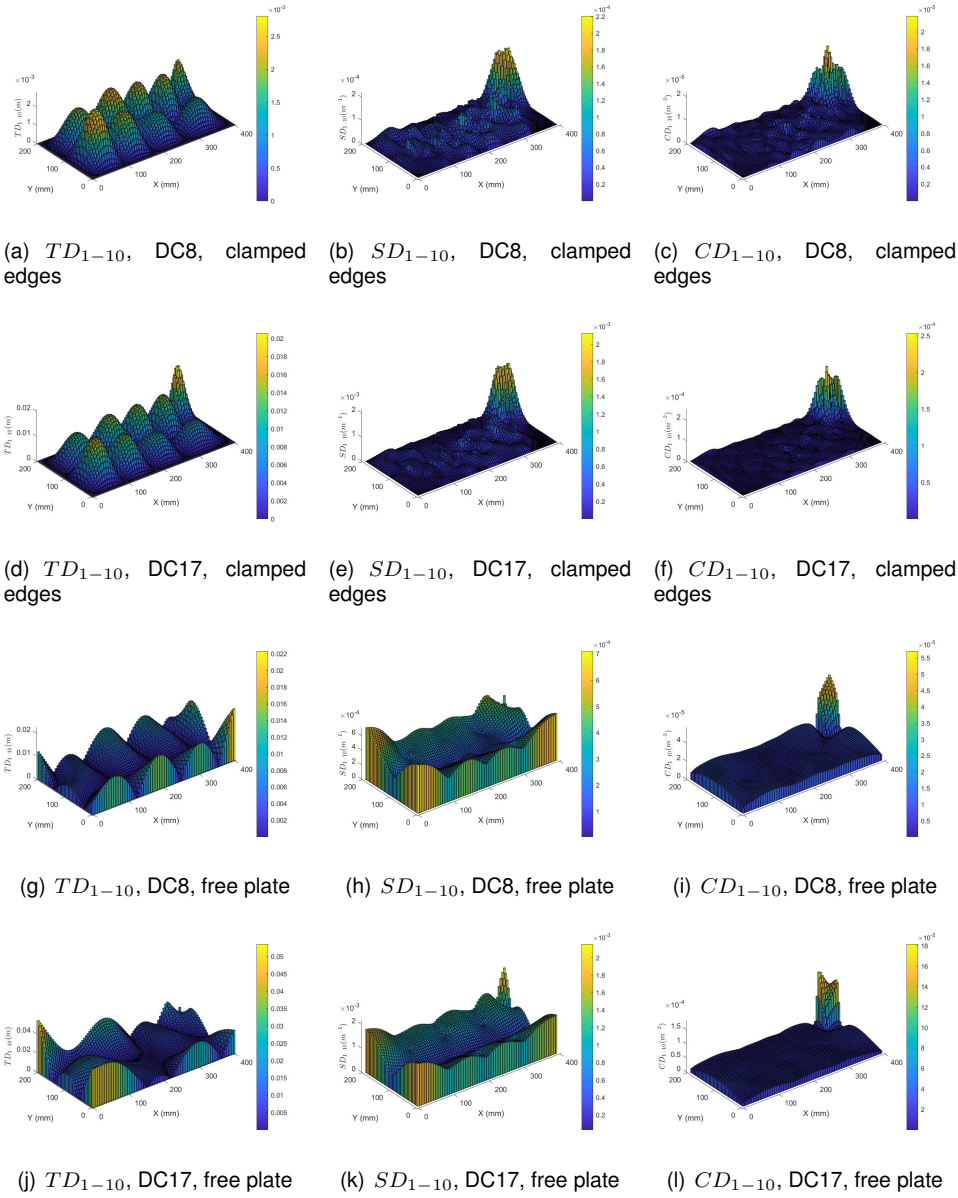

(a) TD_{1-10}, DC8, clamped edges (b) SD_{1-10}, DC8, clamped edges (c) CD_{1-10}, DC8, clamped edges

(d) TD_{1-10}, DC17, clamped edges (e) SD_{1-10}, DC17, clamped edges (f) CD_{1-10}, DC17, clamped edges

(g) TD_{1-10}, DC8, free plate (h) SD_{1-10}, DC8, free plate (i) CD_{1-10}, DC8, free plate

(j) TD_{1-10}, DC17, free plate (k) SD_{1-10}, DC17, free plate (l) CD_{1-10}, DC17, free plate

Figure 4.16: Damage detection with the TD, SD and CD index for DC8 and DC17, and corner damage scenario, for both the plate with clamped edges and the free plate.

4.3.3 Sum of Field Derivatives

This damage indicator has a high degree of similarity to the one shown in Section 4.3.2, with the only differences being the choice of not employing the euclidean norm of all vectorial components of the derivatives - only the x component - and using the first four degrees of derivation, instead of just two. Figures 4.18 and 4.19 show the response of the full derivation degree range to a center damage scenario, with both DC8 and DC17, for the plate with clamped edges and the free one respectively. As before, the higher degree of derivation employed the more noticeable are the disturbances provoked by the damage be, starting especially on the curvatures, with almost no noticeable impact on the displacements and rotations. The mode shapes are noticeably different between the clamped and free plates, and the differences to the previous method are visible, which can be seen by comparing to the rotations

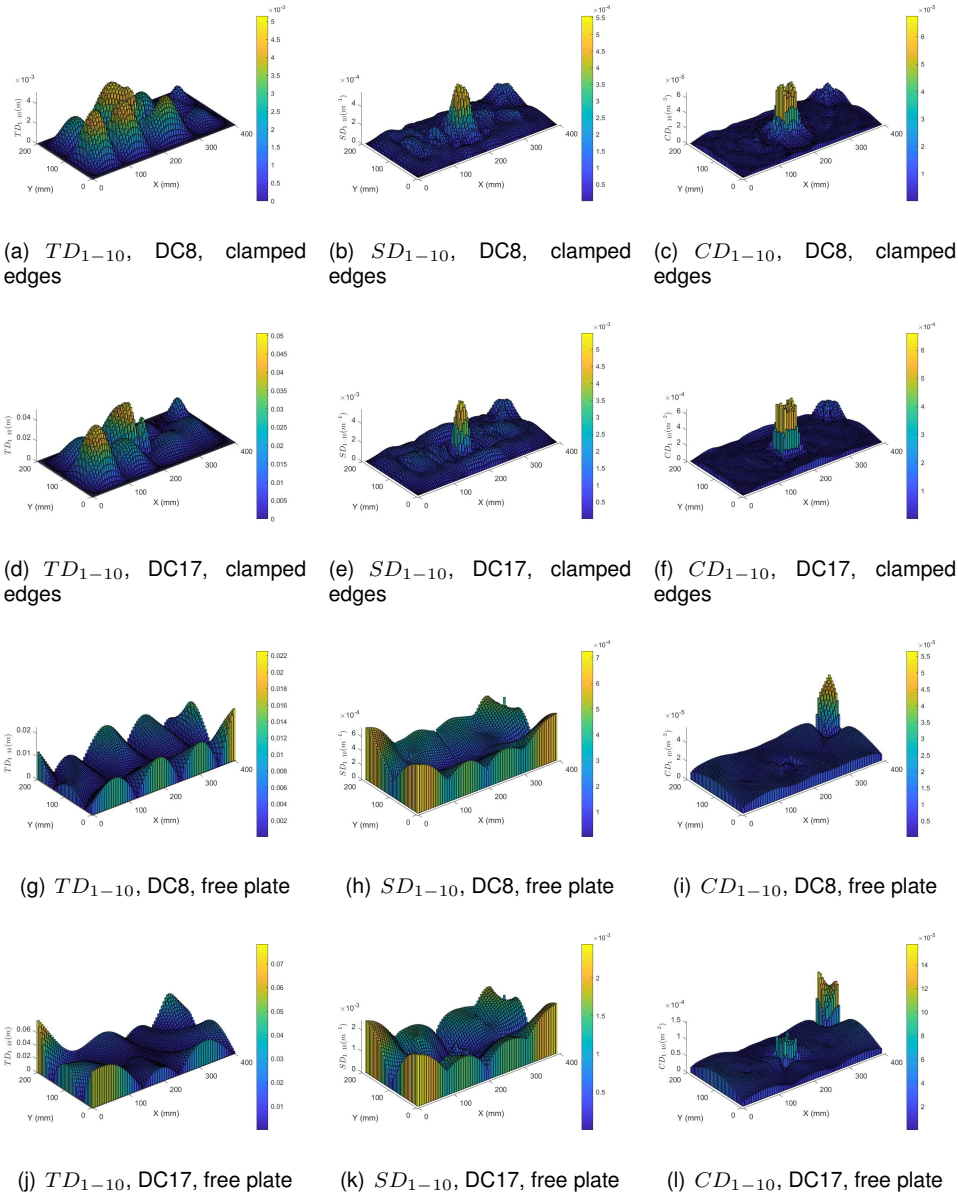

(a) TD_{1-10}, DC8, clamped edges (b) SD_{1-10}, DC8, clamped edges (c) CD_{1-10}, DC8, clamped edges

(d) TD_{1-10}, DC17, clamped edges (e) SD_{1-10}, DC17, clamped edges (f) CD_{1-10}, DC17, clamped edges

(g) TD_{1-10}, DC8, free plate (h) SD_{1-10}, DC8, free plate (i) CD_{1-10}, DC8, free plate

(j) TD_{1-10}, DC17, free plate (k) SD_{1-10}, DC17, free plate (l) CD_{1-10}, DC17, free plate

Figure 4.17: Damage detection with the TD, SD and CD index for DC8 and DC17, and center + corner damage scenario, for both the plate with clamped edges and the free plate.

and curvatures seen on Figures 4.13 and 4.14, which should provide different results for the damage detection. The peaks in the corners of the fourth derivative of the displacements on the free plate are most likely the results of the high sensitivity of this high degree of derivative to a small disturbance on the mode shape, such as a rounding error; the direct consequence that can be foreseen at this instance is that it is as high a disturbance as the one caused by the damaged area of DC8, which would severely impact damage detection when analyzing only the mode shapes.

Just as in the other damage indices, the damage detection is first tested with a center damage scenario, for both damage cases and boundary conditions sets, which can be seen on Figure 4.20. As before, the use of only the displacement fields is mostly unusable for damage detection; and, just as in the use of the TD, SD and CD index, the quality of damage detection using the rotations is hampered when using the free plate. For the curvatures and higher degree derivatives, the detection quality is

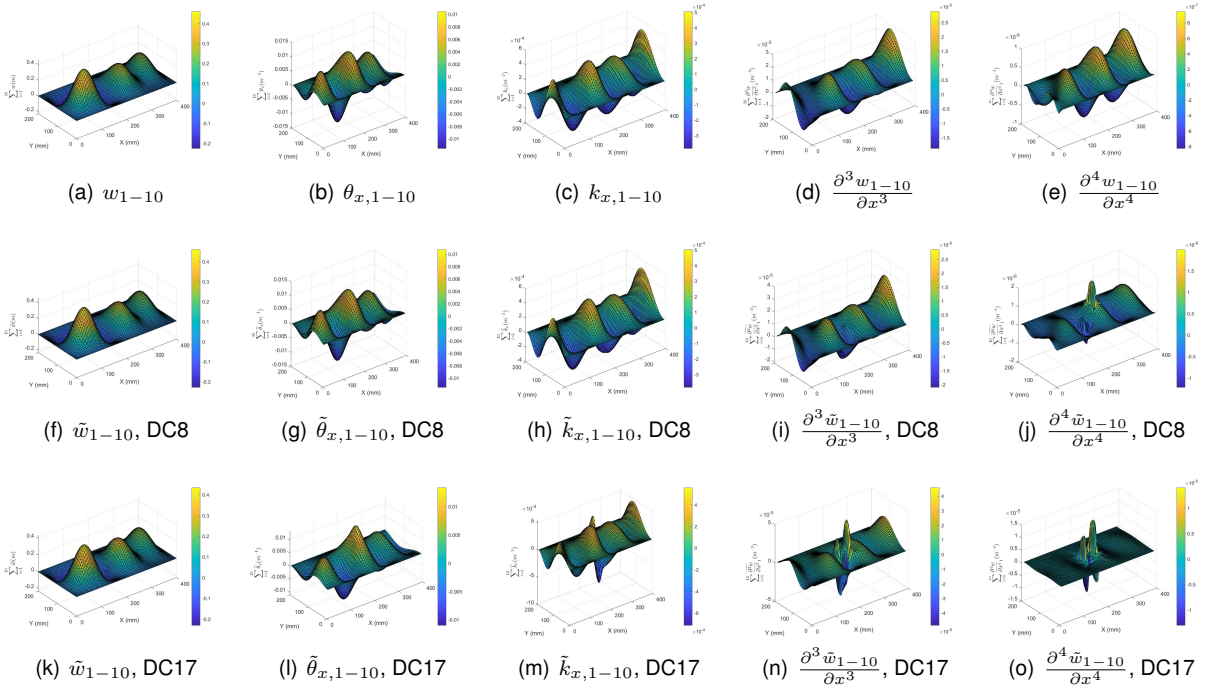

(a) w_{1-10} (b) $\theta_{x,1-10}$ (c) $k_{x,1-10}$ (d) $\frac{\partial^3 w_{1-10}}{\partial x^3}$ (e) $\frac{\partial^4 w_{1-10}}{\partial x^4}$

(f) $\tilde{w}_{1-10}$, DC8 (g) $\tilde{\theta}_{x,1-10}$, DC8 (h) $\tilde{k}_{x,1-10}$, DC8 (i) $\frac{\partial^3 \tilde{w}_{1-10}}{\partial x^3}$, DC8 (j) $\frac{\partial^4 \tilde{w}_{1-10}}{\partial x^4}$, DC8

(k) $\tilde{w}_{1-10}$, DC17 (l) $\tilde{\theta}_{x,1-10}$, DC17 (m) $\tilde{k}_{x,1-10}$, DC17 (n) $\frac{\partial^3 \tilde{w}_{1-10}}{\partial x^3}$, DC17 (o) $\frac{\partial^4 \tilde{w}_{1-10}}{\partial x^4}$, DC17

Figure 4.18: Displacement field and first two derivatives of the undamaged and damaged plate with both DC8 and DC17, and center damage scenario, using the x component of the derivation vectors, for the plate with clamped edges.

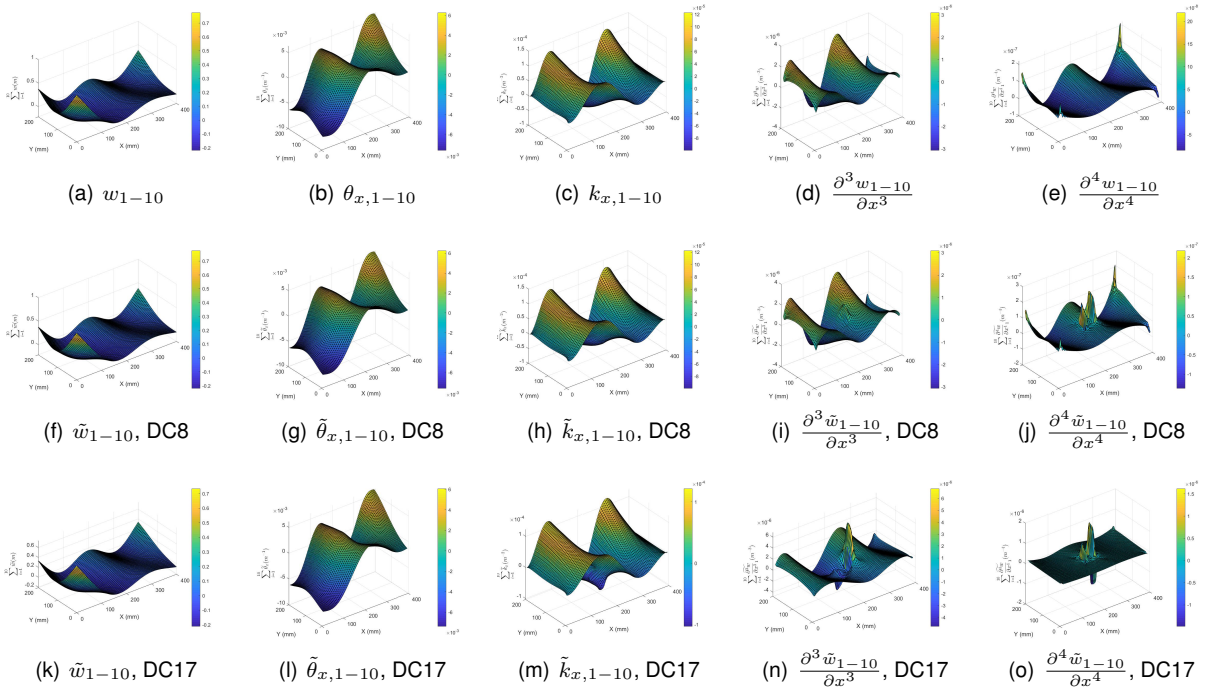

(a) w_{1-10} (b) $\theta_{x,1-10}$ (c) $k_{x,1-10}$ (d) $\frac{\partial^3 w_{1-10}}{\partial x^3}$ (e) $\frac{\partial^4 w_{1-10}}{\partial x^4}$

(f) $\tilde{w}_{1-10}$, DC8 (g) $\tilde{\theta}_{x,1-10}$, DC8 (h) $\tilde{k}_{x,1-10}$, DC8 (i) $\frac{\partial^3 \tilde{w}_{1-10}}{\partial x^3}$, DC8 (j) $\frac{\partial^4 \tilde{w}_{1-10}}{\partial x^4}$, DC8

(k) $\tilde{w}_{1-10}$, DC17 (l) $\tilde{\theta}_{x,1-10}$, DC17 (m) $\tilde{k}_{x,1-10}$, DC17 (n) $\frac{\partial^3 \tilde{w}_{1-10}}{\partial x^3}$, DC17 (o) $\frac{\partial^4 \tilde{w}_{1-10}}{\partial x^4}$, DC17

Figure 4.19: Displacement field and first two derivatives of the undamaged and damaged plate with both DC8 and DC17, and center damage scenario, using the x component of the derivation vectors, for the free plate.

incrementally improved as the derivation degree used is higher, though in diminishing returns, and the free plate still provides slightly lower quality of damage detection. And, as seen previously, the peaks of the damage index are about 10x higher when DC17 is present in comparison to DC8.

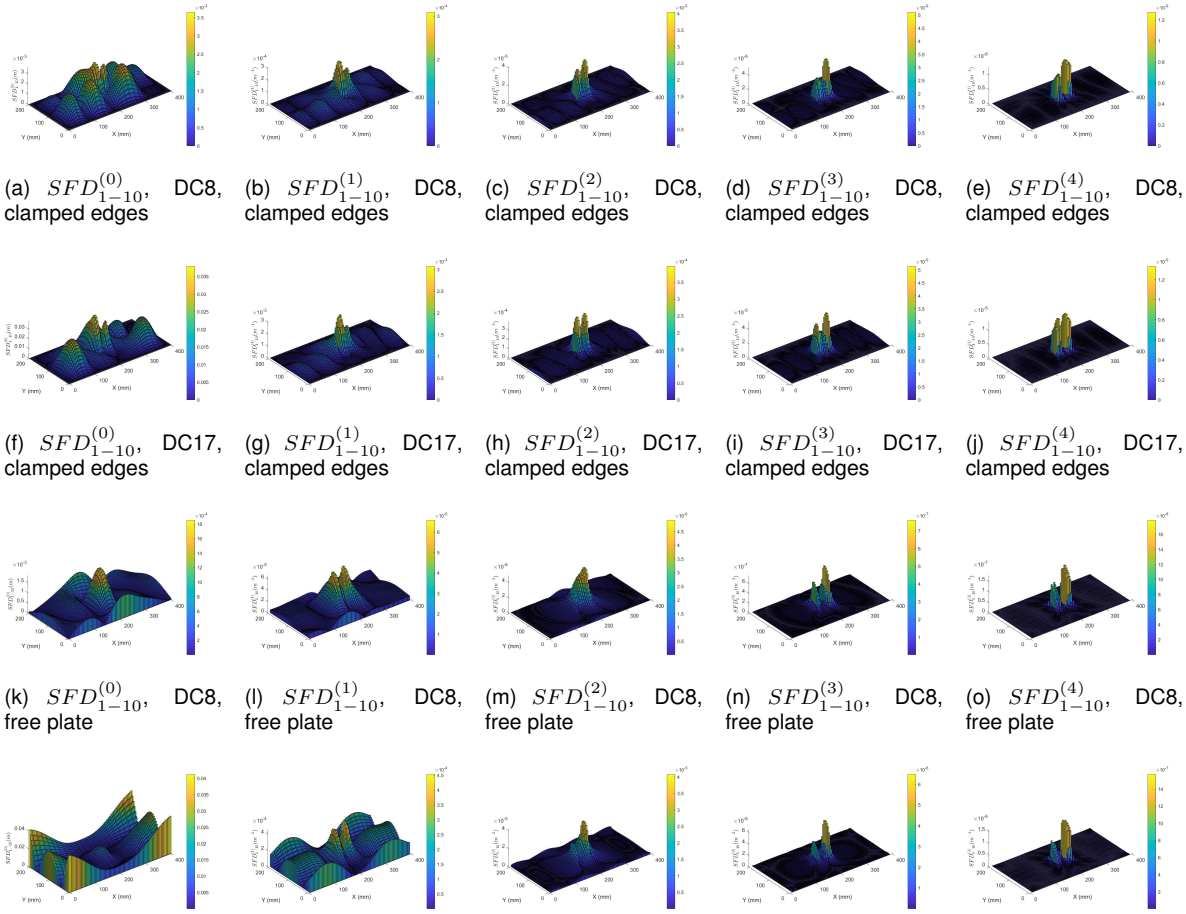

(a) $SFD^{(0)}_{1-10}$, DC8, clamped edges (b) $SFD^{(1)}_{1-10}$, DC8, clamped edges (c) $SFD^{(2)}_{1-10}$, DC8, clamped edges (d) $SFD^{(3)}_{1-10}$, DC8, clamped edges (e) $SFD^{(4)}_{1-10}$, DC8, clamped edges

(f) $SFD^{(0)}_{1-10}$, DC17, clamped edges (g) $SFD^{(1)}_{1-10}$, DC17, clamped edges (h) $SFD^{(2)}_{1-10}$, DC17, clamped edges (i) $SFD^{(3)}_{1-10}$, DC17, clamped edges (j) $SFD^{(4)}_{1-10}$, DC17, clamped edges

(k) $SFD^{(0)}_{1-10}$, DC8, free plate (l) $SFD^{(1)}_{1-10}$, DC8, free plate (m) $SFD^{(2)}_{1-10}$, DC8, free plate (n) $SFD^{(3)}_{1-10}$, DC8, free plate (o) $SFD^{(4)}_{1-10}$, DC8, free plate

(p) $SFD^{(0)}_{1-10}$, DC17, free plate (q) $SFD^{(1)}_{1-10}$, DC17, free plate (r) $SFD^{(2)}_{1-10}$, DC17, free plate (s) $SFD^{(3)}_{1-10}$, DC17, free plate (t) $SFD^{(4)}_{1-10}$, DC17, free plate

Figure 4.20: Damage detection with the DFD method for DC8 and DC17 and center damage scenario, for both the clamped and free plates.

Figure 4.21 shows the use of the SFD index with a corner damage scenario. Just as in the center damage scenario, the use of the displacements is very unreliable for damage detection, and there is a considerable loss of quality in the use of rotations, with a slight advantage for the clamped plate, with DC17. Analyzing the use of the curvatures, the clamped plate shows a higher quality than that of the free plate, and this tendency is maintained as higher degrees of derivative are employed, at a successively lower degree; this may be due to the peaks observed on the corners of the plate when higher order derivatives are employed on the free plate. Just as before, the presence of DC17 produces about 10x higher peak values of the damage index than DC8 on all derivative degrees and boundary conditions.

Figure 4.22 shows the use of the SFD index for damage detection for the multiple damage scenario, with equal damaged areas of 40 mm x 40 mm on the center and corner of the plate. The different boundary conditions highlight each of the damaged areas, with the clamped plate and the free one showing primarily the center and the corner damaged areas respectively; this reinforces the observation made on the end of Section 4.3.2 that the clamped edges may have a strong concealing effect on damage located close to them.

Such as in the TD, SD and CD index, the use of the SFD index is limited by the choice of using

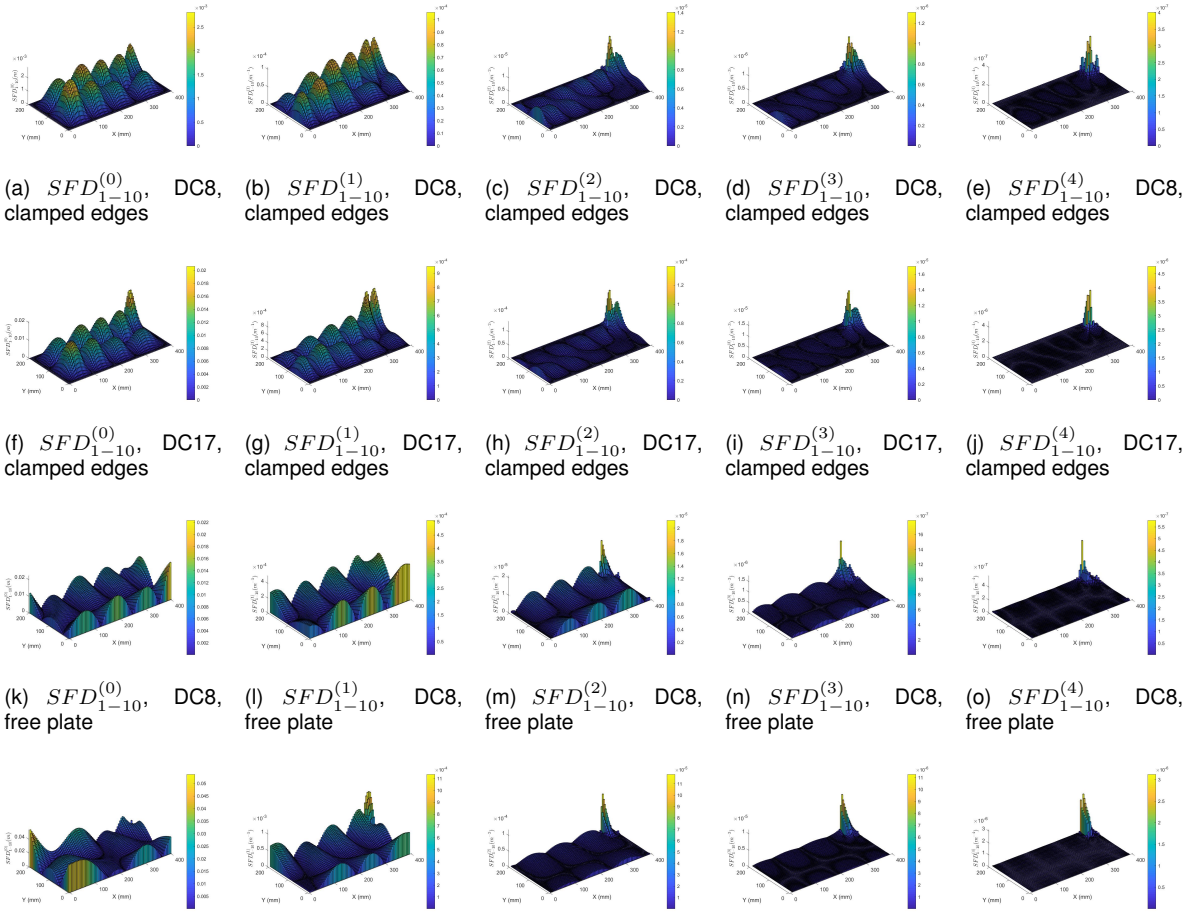

(a) $SFD^{(0)}_{1-10}$, DC8, clamped edges (b) $SFD^{(1)}_{1-10}$, DC8, clamped edges (c) $SFD^{(2)}_{1-10}$, DC8, clamped edges (d) $SFD^{(3)}_{1-10}$, DC8, clamped edges (e) $SFD^{(4)}_{1-10}$, DC8, clamped edges

(f) $SFD^{(0)}_{1-10}$, DC17, clamped edges (g) $SFD^{(1)}_{1-10}$, DC17, clamped edges (h) $SFD^{(2)}_{1-10}$, DC17, clamped edges (i) $SFD^{(3)}_{1-10}$, DC17, clamped edges (j) $SFD^{(4)}_{1-10}$, DC17, clamped edges

(k) $SFD^{(0)}_{1-10}$, DC8, free plate (l) $SFD^{(1)}_{1-10}$, DC8, free plate (m) $SFD^{(2)}_{1-10}$, DC8, free plate (n) $SFD^{(3)}_{1-10}$, DC8, free plate (o) $SFD^{(4)}_{1-10}$, DC8, free plate

(p) $SFD^{(0)}_{1-10}$, DC17, free plate (q) $SFD^{(1)}_{1-10}$, DC17, free plate (r) $SFD^{(2)}_{1-10}$, DC17, free plate (s) $SFD^{(3)}_{1-10}$, DC17, free plate (t) $SFD^{(4)}_{1-10}$, DC17, free plate

Figure 4.21: Damage detection with the DFD index for DC8 and DC17 and corner damage scenario, for both the plate with clamped edges and the free plate.

only the sum of the first ten modes for damage detection, as the different mode shapes are prone to highlighting different damage locations and in this way there is no control or notion of what possible damaged areas could be concealed. The difference in possible blind spots in damage detection between the clamped and the free plates is important to use as a way to anticipate them, however it may not be possible to accommodate for when using these method in the field (for instance, it may not be practical or possible to disassemble a wing from an airplane to detect damage on its root). Generally, the plates clamped on all our edges show better damage detection for lower degree derivatives, when compared to the free plate, however, when the third and fourth derivatives are used, the differences between the results of the different boundary conditions become less noticeable.

There seems to be no detectable difference between using only the derivatives in the x direction and the euclidean norm of the different components, besides the different geometries generated and their potential for better detecting damage in specific locations. The dependence of damage detection on location is substantial when the sum of the results of the first ten modes is employed, *versus* the analysis of every mode separately; for this reason, the simplification obtained by this choice is overshadowed by the much higher versatility and capabilities of the mode-by-mode analysis for most damage scenarios.

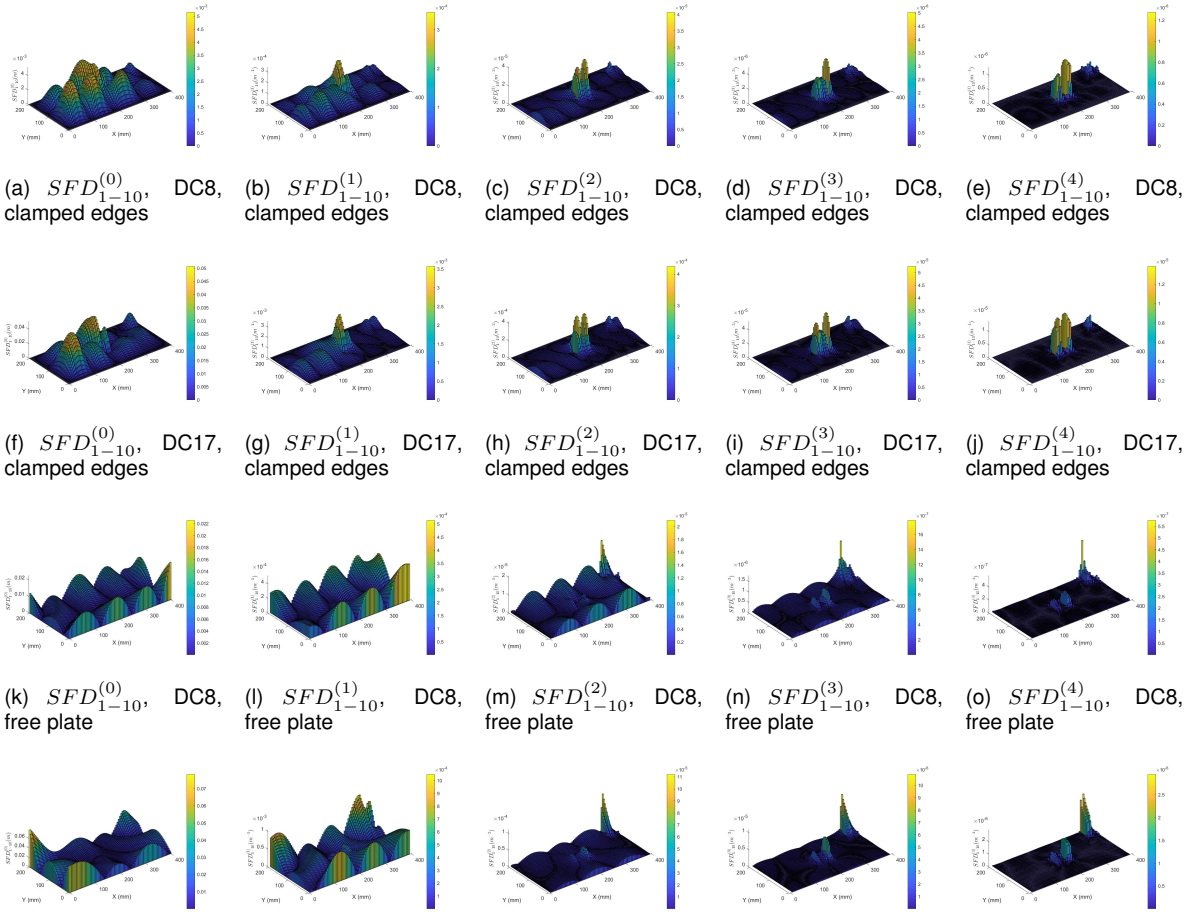

(a) $SFD^{(0)}_{1-10}$, DC8, clamped edges (b) $SFD^{(1)}_{1-10}$, DC8, clamped edges (c) $SFD^{(2)}_{1-10}$, DC8, clamped edges (d) $SFD^{(3)}_{1-10}$, DC8, clamped edges (e) $SFD^{(4)}_{1-10}$, DC8, clamped edges

(f) $SFD^{(0)}_{1-10}$, DC17, clamped edges (g) $SFD^{(1)}_{1-10}$, DC17, clamped edges (h) $SFD^{(2)}_{1-10}$, DC17, clamped edges (i) $SFD^{(3)}_{1-10}$, DC17, clamped edges (j) $SFD^{(4)}_{1-10}$, DC17, clamped edges

(k) $SFD^{(0)}_{1-10}$, DC8, free plate (l) $SFD^{(1)}_{1-10}$, DC8, free plate (m) $SFD^{(2)}_{1-10}$, DC8, free plate (n) $SFD^{(3)}_{1-10}$, DC8, free plate (o) $SFD^{(4)}_{1-10}$, DC8, free plate

(p) $SFD^{(0)}_{1-10}$, DC17, free plate (q) $SFD^{(1)}_{1-10}$, DC17, free plate (r) $SFD^{(2)}_{1-10}$, DC17, free plate (s) $SFD^{(3)}_{1-10}$, DC17, free plate (t) $SFD^{(4)}_{1-10}$, DC17, free plate

Figure 4.22: Damage detection with the DFD index for DC8 and DC17 and center + corner damage scenario, for both the plate with clamped edges and the free plate.

4.4 Frequency Analysis

The difference in frequencies between damaged and undamaged plates is analyzed for different boundary conditions, damage cases, the first ten modes, and different damage placements.

Table 4.1 shows the natural frequencies of the first ten modes for DC8 and DC17 for both the clamped and the free plate with the center damage scenario - f_q for the undamaged plate and ${}^{DC}\tilde{f}_q$ for the damaged plate -, as well as the relative frequency differences - ${}^{DC}\text{FD}_q$. As expected, for all ten modes and both boundary conditions, the natural frequencies of the damaged plate are lower than those of the undamaged one, and the main difference between DC8 and DC17 is that the latter produces larger values of FD as the damage severity is much higher, more so for some modes than others. A possible factor contributing to the difference in FD for different modes could be the mode shapes themselves and their behaviour on the damaged area.

To enable this analysis to be made, the graphs in Figure 4.23 were generated, which show, for each mode, on the primary vertical axis, the average value of the displacements and the euclidean norm of the rotations and curvatures on the damaged area (represented by bars on the graphs) and, on the

Table 4.1: Natural frequency comparison for DC8 and DC17 and center damage scenario

Mode	Clamped Plate					Free plate				
	f_q(Hz)	${}^{8}\tilde{f}_q$(Hz)	${}^{8}\text{FD}_q$	${}^{17}\tilde{f}_q$(Hz)	${}^{17}\text{FD}_q$	f_q(Hz)	${}^{8}\tilde{f}_q$(Hz)	${}^{8}\text{FD}_q$	${}^{17}\tilde{f}_q$(Hz)	${}^{17}\text{FD}_q$
1	159,87	159,64	0,14%	153,92	3,72%	20,91	20,73	0,86%	20,69	1,06%
2	178,93	178,87	0,03%	178,57	0,20%	26,92	26,84	0,32%	26,24	2,54%
3	224,44	223,59	0,38%	216,93	3,35%	50,60	50,59	0,02%	50,58	0,05%
4	301,59	301,29	0,10%	298,74	0,94%	74,26	74,25	0,01%	74,14	0,16%
5	409,54	407,69	0,45%	396,34	3,22%	98,12	97,82	0,31%	97,74	0,38%
6	433,61	433,49	0,03%	426,92	1,54%	145,62	145,28	0,23%	142,84	1,91%
7	446,03	445,48	0,12%	445,12	0,20%	155,66	155,56	0,06%	150,63	3,23%
8	473,75	473,48	0,06%	469,11	0,98%	161,04	161,03	0,01%	160,98	0,04%
9	524,20	522,78	0,27%	521,64	0,49%	168,32	168,27	0,03%	168,18	0,08%
10	546,23	545,20	0,19%	535,35	1,99%	179,60	179,27	0,18%	173,44	3,43%

secondary vertical axis, the corresponding value for ${}^{8}\text{FD}_q$ and ${}^{17}\text{FD}_q$ (represented by lines), which are normalized to one across the ten modes in order to be analysed in the same axis. These graphs are shown to try and find a relation between these quantities and the impact of the damage in the natural frequencies.

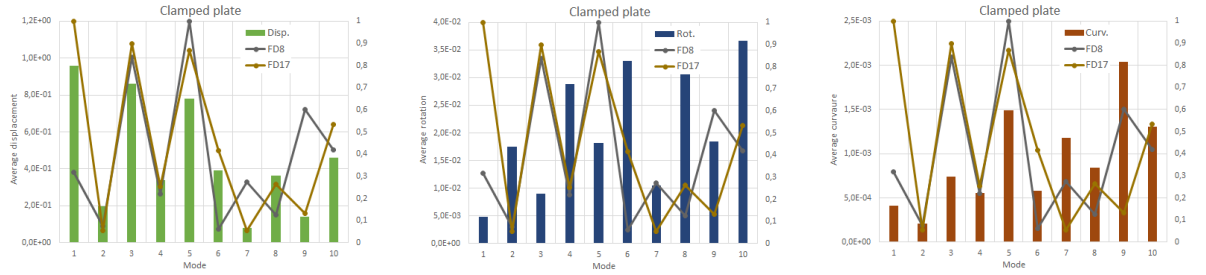

(a) Average displacement on the damaged area for the clamped plate

(b) Average rotation on the damaged area for the clamped plate

(c) Average curvature on the damaged area for the clamped plate

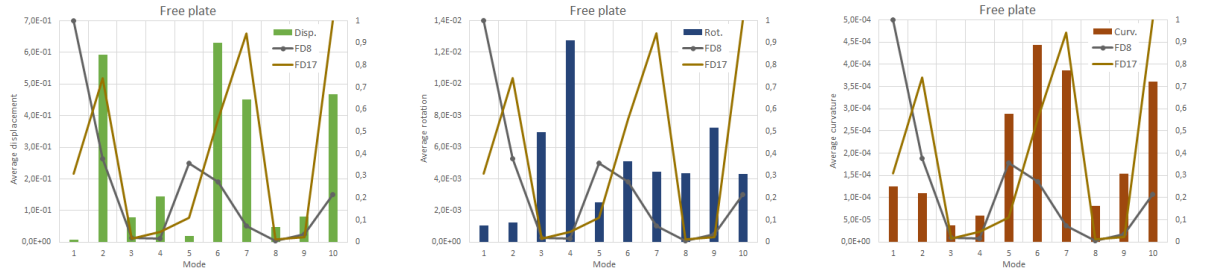

(d) Average displacement on the damaged area for the free plate

(e) Average rotation on the damaged area for the free plate

(f) Average curvature on the damaged area for the free plate

Figure 4.23: Average values of the displacement, rotation, and curvature on the damaged area *vs.* frequency difference for both border conditions and the first ten modes.

For the clamped plate, the relation between ${}^{8}\text{FD}_q$ and ${}^{17}\text{FD}_q$ is largely linear, especially for the first six modes; however for the free plate the behaviour of FD changes significantly between damage cases. Analysing the six sub-figures in Figure 4.23, the displacement at the damaged area shows a strong correlation with the value of ${}^{17}\text{FD}_q$ for all ten modes, and a weaker one with ${}^{8}\text{FD}_q$. These results suggest that, for a severe enough damage case, this correlation could be used to locate damage in

a situation where the only accurate measurement being made of a damaged plate was the that of the natural frequencies, such as a field application, and the mode shapes of the undamaged plate should be known either in advance or through simulations. However, the disparity between ${}^{8}\mathrm{FD}_q$ and ${}^{17}\mathrm{FD}_q$ suggests that, for some situations - especially those with small severity of damage -, this method may not be suitable for locating damage. For damage detection without location, the analysis of the values of FD could be used by itself, depending on the precision of the measurement of the natural frequencies of both the original undamaged plate and the damaged plate, as positive values of FD imply the presence of damage.

4.5 Influence of noise on damage detection

This analysis is made in two complementary approaches: a qualitative analysis of the generated figures for the damage detection and a statistical analysis of the behaviour of the quality index μ according to different noise levels. The pairing of these two approaches is essential to determine the value of μ which constitutes the threshold between a valid damage detection and a corrupted one. For the first approach to this analysis, the center damage scenario is used, with damage case 8 and clamped edges. The noise level is tested for 22 different values between 0 and 10000. The SFD method is used, in order to test all four degrees of derivation and eliminate the variation of damage detection quality achieved by the different modes.

Figure 4.24 shows the behaviour of the displacement field and the four derivatives to several noise levels within the range tested. The displacement and rotation fields show a high resiliency to the introduced noise, as even with the highest noise level tested they are still fairly clear, more so for the displacement than the rotation; these two value fields are shown without noise, with the maximum noise level and with an intermediate one, to illustrate the progression. For the curvatures, and the third and fourth derivatives of the displacement, the noise has a much more noticeable impact on the results for lower and lower noise levels as the order of derivation increases; for these cases, the shown figures are with no noise and the two noise levels which are considered to constitute the border between discernible and indiscernible shapes, when comparing to the clean case. The difference in the sensitivity of the different derivation degrees to the introduced noise is notorious, even if it is considered that the point at which the clarity of the shapes has been lost is subjective, as the noise levels where this happens are considerably different.

Figure 4.25 shows the response of the SFD index to the different noise levels; the choice of the figures follows the same criterion as the previous case, where the derivatives' responses to the noise are shown. The choice of the noise levels is, the same as before, subjective; however the noise levels shown here are smaller than the ones in Figure 4.24, as the damage detection seems to require a greater degree of clarity to analyze than the shapes of the spatial derivatives. The quality indices of the cases shown are, for the borderline detectable damage, very similar: the critical quality index, i.e. the minimum allowed for what is considered a successful damage detection response to damage, can then be defined as $\mu_c = 0.85$. This value is biased towards maintaining a slightly higher detection quality than

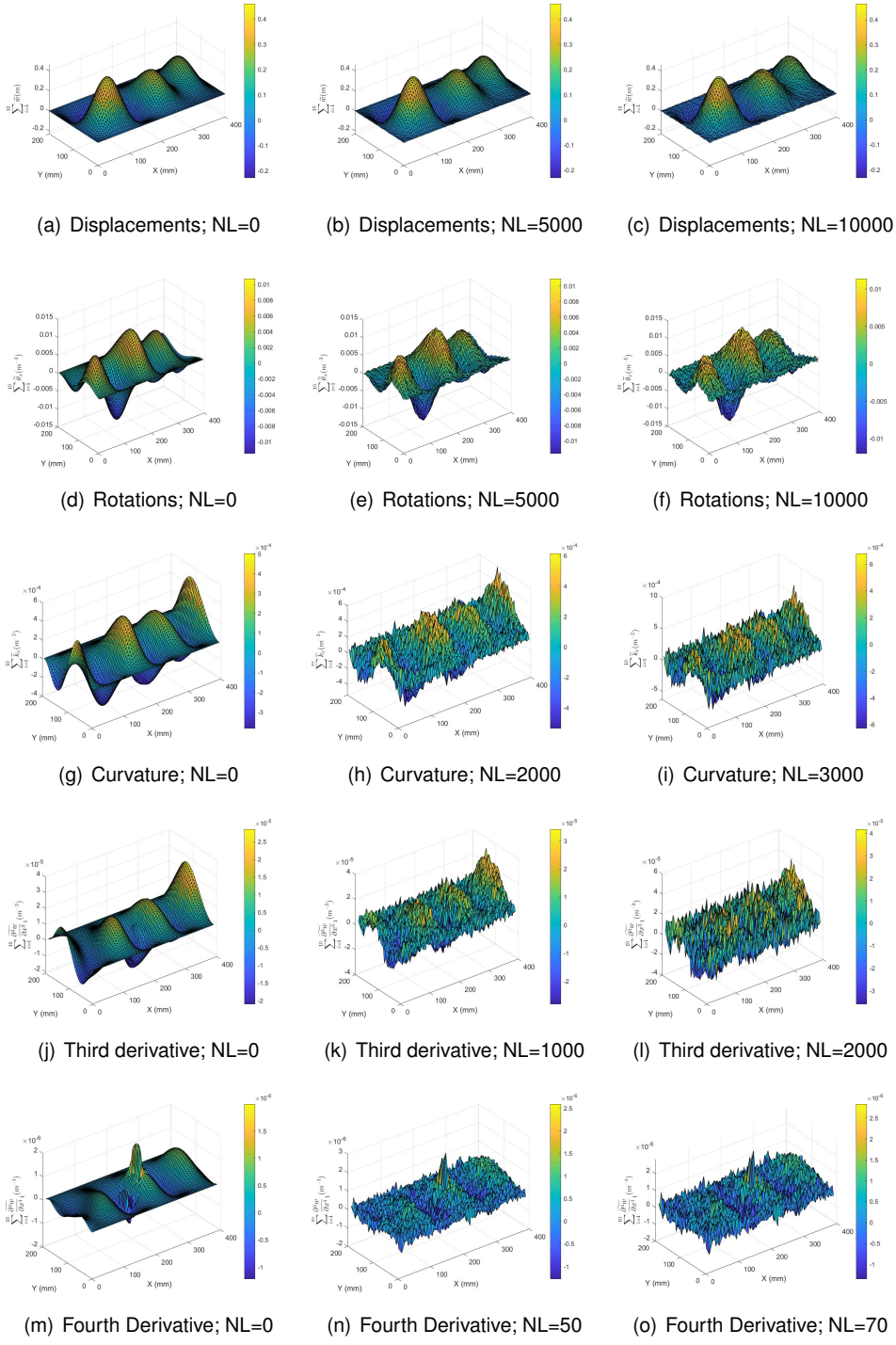

(a) Displacements; NL=0 (b) Displacements; NL=5000 (c) Displacements; NL=10000

(d) Rotations; NL=0 (e) Rotations; NL=5000 (f) Rotations; NL=10000

(g) Curvature; NL=0 (h) Curvature; NL=2000 (i) Curvature; NL=3000

(j) Third derivative; NL=0 (k) Third derivative; NL=1000 (l) Third derivative; NL=2000

(m) Fourth Derivative; NL=0 (n) Fourth Derivative; NL=50 (o) Fourth Derivative; NL=70

Figure 4.24: The four derivation degrees employed and their response to the noise levels, for Damage Case 8.

what is shown in some of the figures.

To evaluate whether the value of μ_c changes significantly for different damage severity cases, the same test is conducted for several values of $d^{(e)}$, using the RLS damage model, and different damage scenarios, however only for only one damaged area. Figure 4.26 shows examples of different combinations of damage scenario, derivative order and damage severity for the borderline detectable damage, as in the previous cases; as before, the value of μ_c, however subjective, is considered to be constant for

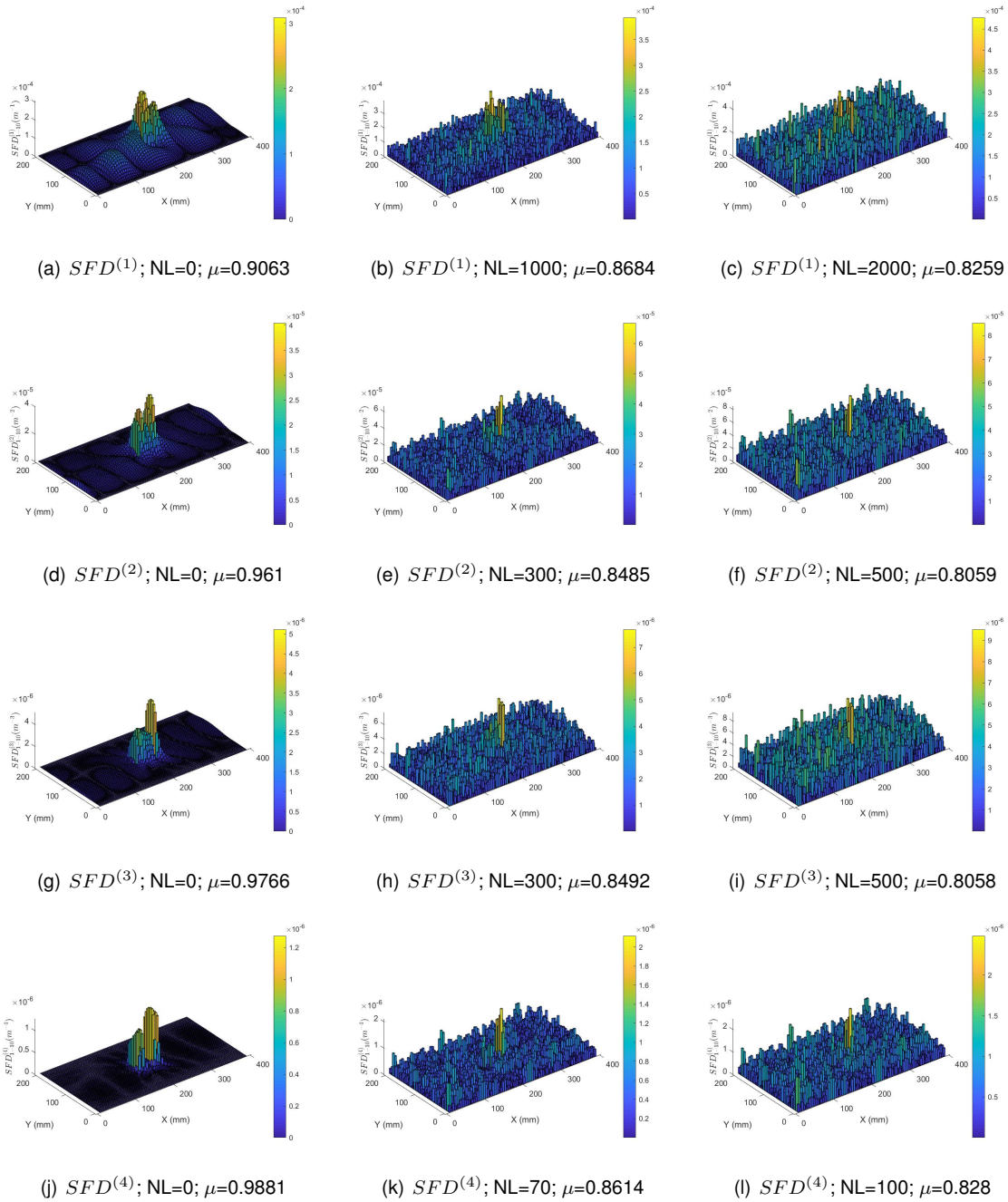

(a) $SFD^{(1)}$; NL=0; μ=0.9063 (b) $SFD^{(1)}$; NL=1000; μ=0.8684 (c) $SFD^{(1)}$; NL=2000; μ=0.8259

(d) $SFD^{(2)}$; NL=0; μ=0.961 (e) $SFD^{(2)}$; NL=300; μ=0.8485 (f) $SFD^{(2)}$; NL=500; μ=0.8059

(g) $SFD^{(3)}$; NL=0; μ=0.9766 (h) $SFD^{(3)}$; NL=300; μ=0.8492 (i) $SFD^{(3)}$; NL=500; μ=0.8058

(j) $SFD^{(4)}$; NL=0; μ=0.9881 (k) $SFD^{(4)}$; NL=70; μ=0.8614 (l) $SFD^{(4)}$; NL=100; μ=0.828

Figure 4.25: The four derivation degrees employed and their response to the noise levels, for Damage Case 8 and center damaged area, using the sum of the first ten modes

the SFD method at 0.85.

Having established a correlation between the quality index μ and the quality of the damage detection for a single damaged area, a statistical analysis can then be made to quantitatively evaluate the impact of the presence of noise in the damage detection, as described in Section 3.2.2. Figure 4.27 shows the behaviour of the quality index for different values of the Noise Level, for DC8 and DC17, which constitute different severity levels of damage. The two graphs show the same behaviour of the damage detection method for both damage cases in response to noise, only with a skew to the right for the more severe one, i.e. DC17. This skew shows a higher threshold of noise level at which the damage detection can

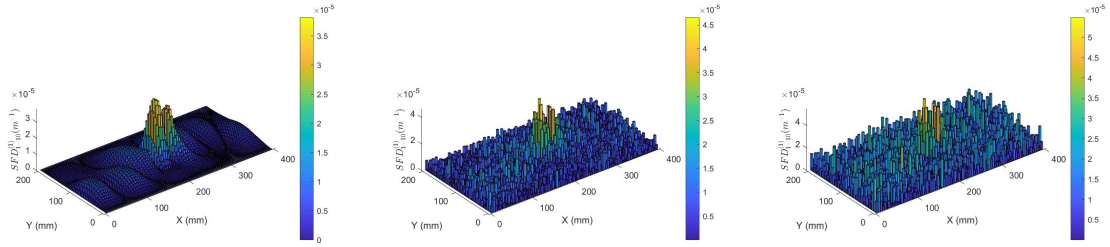

(a) $SFD^{(1)}$; $d^e = 0.02$; Center damage; NL=0; μ=0.9182

(b) $SFD^{(1)}$; $d^e = 0.02$; Center damage; NL=100; μ=0.8939

(c) $SFD^{(1)}$; $d^e = 0.02$; Center damage; NL=200; μ=0.8579

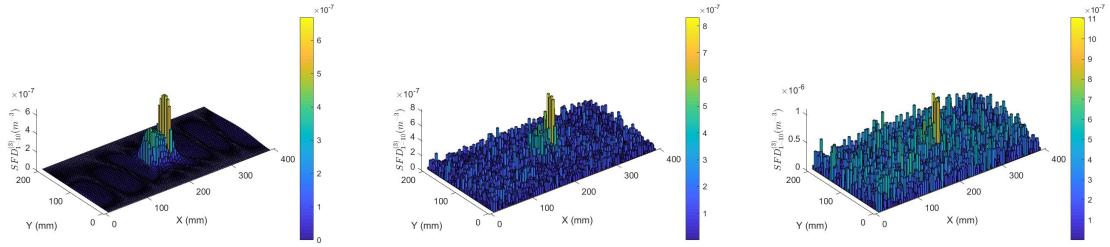

(d) $SFD^{(3)}$; $d^e = 0.02$; Center damage; NL=0; μ=0.9782

(e) $SFD^{(3)}$; $d^e = 0.02$; Center damage; NL=20; μ=0.9196

(f) $SFD^{(3)}$; $d^e = 0.02$; Center damage; NL=50; μ=0.86

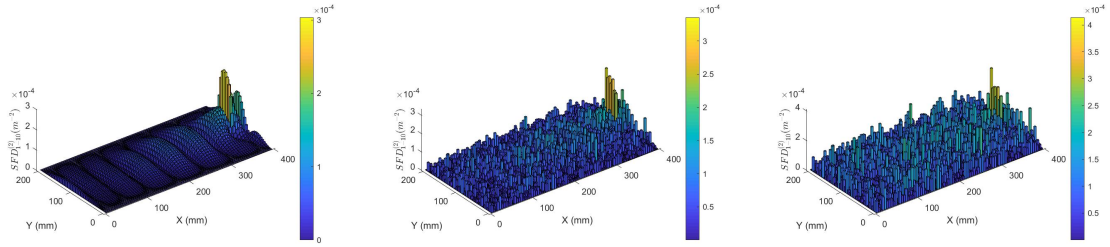

(g) $SFD^{(2)}$; $d^e = 0.7$; Edge damage; NL=0; μ=0.9247

(h) $SFD^{(2)}$; $d^e = 0.7$; Edge damage; NL=1000; μ=0.8964

(i) $SFD^{(2)}$; $d^e = 0.7$; Edge damage; NL=2000; μ=0.8703

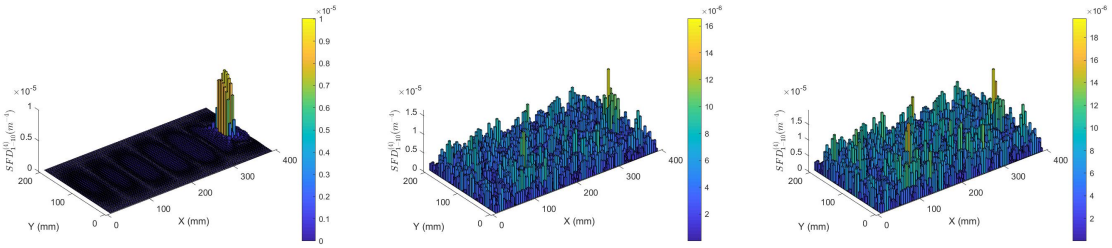

(j) $SFD^{(4)}$; $d^e = 0.7$; Edge damage; NL=0; μ=0.9893

(k) $SFD^{(4)}$; $d^e = 0.7$; Edge damage; NL=700; μ=0.8686

(l) $SFD^{(4)}$; $d^e = 0.7$; Edge damage; NL=1000; μ=0.843

Figure 4.26: Damage detection with different damage placements, severity, and noise level, for detection quality close to μ_c.

work, of about 10x, which is expected, as the maximum SD and CD shown in Figure 4.5 also have this difference between the two damage cases. Each curve represents a specific order of derivative being used in the SFD index, and the horizontal black line is a visualization of $\mu_c = 0.85$, to better analyze the points at which the damage detection methods stop producing good results.

The data presented in this Section clearly shows that higher derivative degrees have a higher sensibility to noise; in parallel, this sensitivity may be the exact reason why the damage detection is clearer

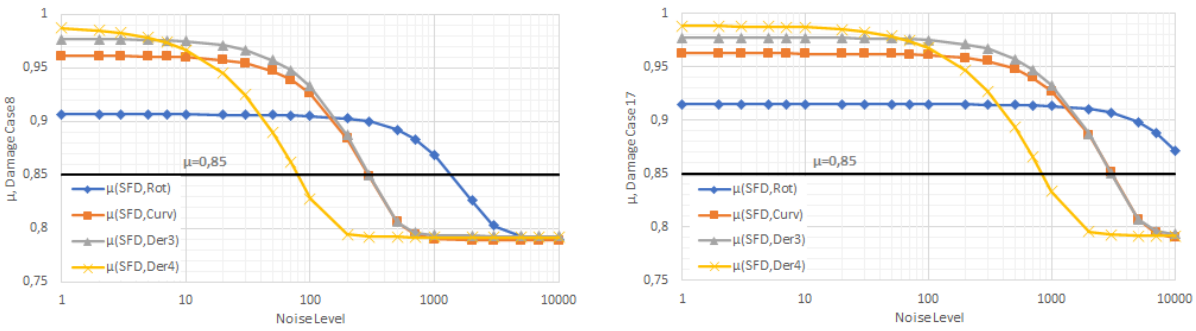

(a) Damage Case 8

(b) Damage Case 17

Figure 4.27: Behaviour of the quality index for different values of the Noise Level, and for two different damage cases

and more effective when higher derivative degrees are employed, as both noise and damaged areas represent perturbations in the displacement fields, although one is dispersed through the plate and the other localized. For damage cases less severe than the ones used in these simulations, the precision of the results may come into play in a form similar to the randomly generated noise, however for a double precision data set such as the one being used here these damage cases could be considered not severe enough to warrant detectability.

4.6 Influence of damage depth in the plate on damage detection

The tests performed so far are simulations where the damage is considered to impact all plies in a specified location, throughout the plate thickness. Considering field applications, this analysis is of extreme importance, as the damages found can be of many different types, including those limited to internal or specific depths, which might be more difficult to be visually detected.

In order to study the connection between damage depth and its detectability, the maximum value of the SFD index found on the plate is used, as before to establish damage severity. Six simulations are run, in each of which a center damage scenario of DC8 is applied to one of the plies. Figure 4.28 shows a clear correlation, for all degrees of the index, where the depth hampers the damage detection - when the damage is applied to the center plies of the plate, the maximum index is smaller by a factor of 10 to 100. As the damage index used here uses the sum of the first ten modes for damage detection, the modes' direction of strain at the damaged area and the plies' fiber orientation can be considered as not having an influence on the results. The perceived cause of this correlation is the fact that the neutral line position in the laminate, while not fixed for all modes, is generally close to the center, and as such the reduction in stiffness has the least impact when there is less load applied.

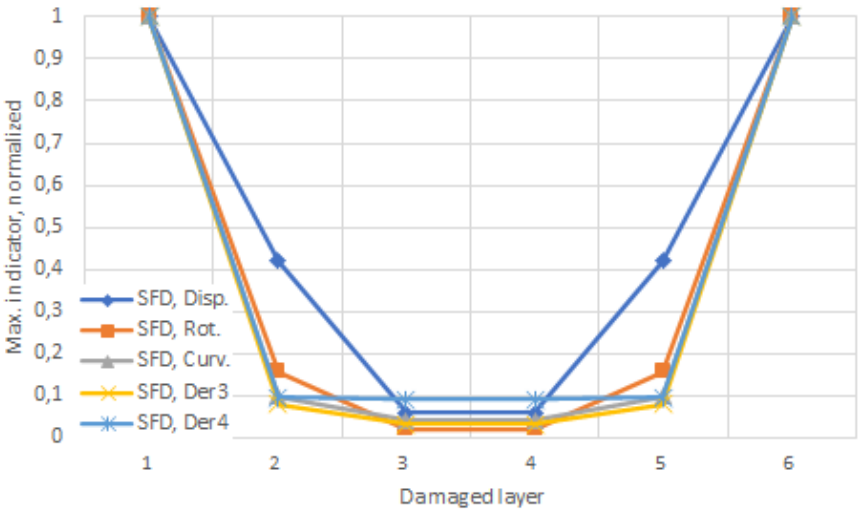

Figure 4.28: Damage severity according to damage depth.

Having in mind the motivation of this analysis - the lower visibility of damage in the plies closer to the center of the plate -, these results show how modal analysis, in the form that is proposed in this thesis, may not be the most suitable solution to detect this type of damage.

Chapter 5

Conclusions

5.1 Achievements

The main goal of this thesis was to further the development of techniques that can more effectively detect and locate damage in composite structures, which have been taking an increasingly more important role in the forefront of engineering, and as such need an equally advanced set of structural health monitoring practices. The study of the vibrational behaviour of plates, namely through mode shapes and natural frequencies, has the potential of being a valuable tool in this regard. Regarding these objectives, a high degree of success can be claimed, as several aspects of the use of these techniques are here well established and studied for a rectangular plate.

The implementation of the Finite Element Model for the study of different variables, such as Damage Cases, Damage Scenarios, and boundary conditions, was successfully developed using Ansys® software, with meaningful differences found in the approaches, allowing a deeper understanding of the behaviour of the plate when damage is present, as well as its response to the different variables at hand. The APDL® software's ability to accept input files to run Finite Element simulations also allowed the fulfilment of a large array of simulations.

The use of spatial derivatives through the finite difference method, motivated by a number of examples in the literature, was shown to be invaluable in highlighting the small disturbances caused by damaged areas in the mode shapes, which would otherwise hardly be detectable. Although some difficulties were found in the implementation of this technique, mainly in establishing a uniform grid of nodes, its use was proven to be a reliable indicator of the damage severity, as well as an indirect indicator of the data quality, through the noise sensitivity observed in the higher order derivatives, parallel to the main use in the damage indices. The detection of damage just by the disturbances in the shapes of the higher order derivatives value fields is a clear manifestation of their sensitivity and can be considered for damage location by itself for high severity damage cases.

The damage indices were tested for a number of different variables, having in mind the distinct choices made in their conception. Regarding the use of one or all components of the derivatives' vectors, no clear advantage in damage detection was observed for either option, besides the slight simplification

in the calculations when using only the x component. Performing the analysis mode-by-mode or on the average of the first ten modes is a choice which was shown to have a considerable impact in damage detection, due to the high tendency that some mode shapes have of highlighting some damaged areas more than others, more clearly observed in the multiple damage scenarios; if the damage index of choice can be analyzed for each mode, the chances of this type of concealment are much lower. The number of derivative degrees employed was also shown to have a high impact on damage detection, as less severe damage cases have the potential to only be detectable when higher order derivatives are employed, due to their higher sensitivity. The employment of different boundary conditions showed, most of all, how the clamped areas of the plate have a high potential of generating blind spots due to the restricted translations on the generated mode shapes; in the work developed, this was verified in the context of multiple damage scenarios, however the presence of noise and/or low severity damaged areas could produce the same effect. This factor is the highest hindrance found for damage detection when testing the damage indices.

The different damage models studied served the main purpose of producing two distinct damage cases to test the response of the damage detection methods to different levels of severity in the damage. However the analysis of the severity of all damage cases considered showed the different impact that the manipulation of each of the elastic constants has on the severity of the damage: G_{12}, E_2, and E_1 have an ascending impact on the strength of the composite, by this order, and the Microphenomenology analysis made by Ladevèze and Lubineau [20] should contribute to the insight that this can bring to the manufacturing process of composite materials.

The frequency analysis also showed promising results in the localization of damaged areas. Besides the expected results of the damaged plate producing lower natural frequencies that the undamaged one, these results show a possible approach to damage localization through the use of natural frequencies alone. However, the application of this method in a practical application is paramount to validate these results, as a high degree of precision in the capture of the natural frequencies is needed for them to work.

The noise simulation is considered to have produced very satisfactory results. The higher sensitivity of the higher order derivatives to the noise, making the damage detection more difficult or impossible past certain points, is a good insight on how these damage indices could perform on real world applications. As the noise in these applications may not behave as evenly as the one generated, an analysis of different derivative degrees, modes, and other variables available, is always valuable to distinguish between different sources of error.

The introduction of damage in only one layer of the laminate highlighted the higher degree of difficulty in detecting damage towards the center of the plate. This information shows a clear weakness of the chosen methods regarding this type of damage, moreover as it is predicted to also be harder to detect by simple visual inspection. What remains to be known is whether alternative methods, either based on modal analysis or not, could be the response to this shortcoming.

A definitive conclusion regarding the use of these damage detection methods for damage quantification was not drawn. As the severity of the damage is always evaluated in comparison with different

damage cases, each intended application should have thresholds based on the available measurements for evaluating whether a given damaged structure is within operating parameters, or alternatively rely on the proposed methods solely for damage detection and have complementary ones for quantification on the detected damaged areas.

5.2 Future Work

For future work in this area, an important first step in adapting these techniques to field application is ensuring a complete set of structural health monitoring practises, which include the recording of undamaged structures' natural frequencies and mode shapes. This way, when the measurements of structures under maintenance are performed, a reliable baseline is available, as not to rely only on FE simulations. The importance of precise measurements is covered in this thesis, unlike the selection of proper equipment and data collection practises, however this aspect is of vital importance to allow these techniques to give accurate and reliable answers.

Future work should also include a more comprehensive study of different element sizes, as one of the main constraints considered in the work developed here was the computation time, which has the potential to be less of an limitation when undergoing more exhaustive research in this area.

The adaptation of these techniques for more complex structures is also an important focus for future work, as the approach made here is only directly valid for approximately 2D or 1D structures - such as plates or beams -, as it's limited by the calculation of the spatial derivatives and its dependency on a uniform 2D grid of nodal values. Although the analysis of plates is highly valuable in itself - as established in Chapter 1 -, as these techniques are refined in this environment a parallel effort should be made to apply them in more real-world applications and a greater variety of engineering structures or structural elements.

Bibliography

[1] A. B. Strong. *Fundamentals of Composites Manufacturing - Materials, Methods, and Applications*. Society of Manufacturing Engineers (SME), 2nd edition edition, 2008. ISBN 9781613449882.

[2] J. Hale. Boeing 787 from the ground up, 2008. URL `https://www.boeing.com/commercial/aeromagazine/articles/qtr_4_06/article_04_2.html`. [Online; accessed 26-October-2021].

[3] Documents: Mclaren p1^{TM}, 2021. URL `https://cars.mclaren.press/ww/press-kits/mclaren-p1#documents`. Construction tab, [Online; accessed 27-October-2021].

[4] D. Adams. Health monitoring of structural material and components. *Health Monitoring of Structural Materials and Components: Methods with Applications*, pages 1–460, 05 2007. doi: 10.1002/9780470511589.

[5] Y. Zou, L. Tong, and G. Steven. Vibration-based model-dependent damage (delamination) identification and health monitoring for composites structures. *Journal of Sound and Vibration*, 230(2): 357–378, 2000. ISSN 0022-460X. doi: https://doi.org/10.1006/jsvi.1999.2624.

[6] J. Araújo dos Santos, H. Lopes, M. Vaz, C. Mota Soares, C. Mota Soares, and M. de Freitas. Damage localization in laminated composite plates using mode shapes measured by pulsed tv holography. *Composite Structures*, 76(3):272 – 281, 2006. ISSN 0263-8223. doi: https://doi.org/10.1016/j.compstruct.2006.06.034.

[7] A. Pandey, M. Biswas, and M. Samman. Damage detection from changes in curvature mode shapes. *Journal of Sound and Vibration*, 145(2):321–332, 1991. ISSN 0022-460X. doi: https://doi.org/10.1016/0022-460X(91)90595-B.

[8] P. Moreno-García, J. Araújo dos Santos, and H. Lopes. A new technique to optimize the use of mode shape derivatives to localize damage in laminated composite plates. *Composite Structures*, 108:548 – 554, 2014. ISSN 0263-8223. doi: https://doi.org/10.1016/j.compstruct.2013.09.050.

[9] M. Abdel Wahab and G. De Roeck. Damage detection in bridges using modal curvatures: Application to a real damage scenario. *Journal of Sound and Vibration*, 226(2):217–235, 1999. ISSN 0022-460X. doi: https://doi.org/10.1006/jsvi.1999.2295.

[10] T. M. Whalen. The behavior of higher order mode shape derivatives in damaged, beam-like structures. *Journal of Sound and Vibration*, 309(3–5):426–464, 2008.

[11] E. Sazonov and P. Klinkhachorn. Optimal spatial sampling interval for damage detection by curvature or strain energy mode shapes. *Journal of Sound and Vibration*, 285(4):783–801, 2005. ISSN 0022-460X. doi: https://doi.org/10.1016/j.jsv.2004.08.021.

[12] S. Dincal and N. Stubbs. Nondestructive damage detection in euler–bernoulli beams using nodal curvatures—part ii: Field measurements. *Structural Control and Health Monitoring*, 21, 03 2014. doi: 10.1002/stc.1564.

[13] D. Feng and M. Feng. Output-only damage detection using vehicle-induced displacement response and mode shape curvature index. *Structural Control and Health Monitoring*, 23, 12 2015. doi: 10.1002/stc.1829.

[14] D. Chen, Y. Xu, and W. Zhu. Experimental investigation of notch-type damage identification with a curvature-based method by using a continuously scanning laser doppler vibrometer system. *Journal of Nondestructive Evaluation*, 36, 05 2017. doi: 10.1007/s10921-017-0418-4.

[15] M. Dahak, N. Touat, and M. Kharoubi. Damage detection in beam through change in measured frequency and undamaged curvature mode shape. *Inverse Problems in Science and Engineering*, 27:1–26, 02 2018. doi: 10.1080/17415977.2018.1442834.

[16] S. S. Naidu and C. Ratnam. Delamination identification on frp composites using normalized modal curvature delamination. *International Journal of Mechanical and Production Engineering Research and Development (IJMPERD)*, 10:679–690, 2020. ISSN 2249-6890. doi: 10.1016/j.compstruct.2015.04.021.

[17] J. Reddy. *Mechanics of Laminated Composite Plates and Shells*. CRC Press, 2^{nd} edition, 1997. ISBN:0-8493-1592-1.

[18] S. S. Rao. *Mechanical Vibrations*. Prentice Hall, 5^{th} edition, 2011. ISBN:978-0132128193.

[19] J. Reddy. *An Introduction to the Finite Element Method*. McGraw-Hill, 3^{rd} edition, 2006. ISBN:007-124473-5.

[20] P. Ladevèze and G. Lubineau. On a damage mesomodel for laminates: micromechanics basis and improvement. *Mechanics of Materials*, 35(8):763–775, 2003. ISSN 0167-6636. doi: 10.1016/S0167-6636(02)00204-1. Multi-scale Modeling of Materials.

[21] Overview of materials for polytetrafluoroethylene (ptfe), extruded, 2021. URL `http://www.matweb.com/search/datasheet_print.aspx?matguid=4e0b2e88eeba4aaeb18e8820f1444cdb`. [Online; accessed 12-April-2021].

[22] H. Lopes, J. Ribeiro, and J. Santos. Interferometric techniques in structural damage identification. *Shock and Vibration*, 19:835–844, 2012. doi: 10.3233/SAV-2012-0692.

[23] K. E. Atkinson. *An Introduction to numerical analysis*. John Wiley and Sons, 2^{nd} edition, 1989. ISBN:0-471-62489-6.

[24] T. Oliveira. Composite plate simulation and damage detection. Online; retrieved 16-December-2021, 2021. URL https://www.mathworks.com/matlabcentral/fileexchange/103670-composite-plate-simulation-and-damage-detection.

[25] M. R. Scatterbar3. Online; retrieved 7-June-2021, 2021. URL https://www.mathworks.com/matlabcentral/fileexchange/1420-scatterbar3.

[26] P. Moreno-García, H. Lopes, and J. Araújo dos Santos. Application of higher order finite differences to damage localization in laminated composite plates. *Composite Structures*, 156:385 – 392, 2016. ISSN 0263-8223. doi: https://doi.org/10.1016/j.compstruct.2015.08.011.

[27] D. F. Adams, L. A. Carlson, and R. B. Pipes. *Experimental Characterization of Advanced Composite Materials*. CRC Press, 3^{rd} edition, 2002. ISBN:978-1587161001.